Research Square

Preprints are preliminary reports that have not undergone peer review.
They should not be considered conclusive, used to inform clinical practice,
or referenced by the media as validated information.

Beyond the Antiviral Echo: Multi-Layer Transcriptomics Reveals Splicing-Centered Remodeling of the RNA-Processing Machinery during Zika Virus Infection of Glioblastoma Stem Cells

Israel Nunes Silveira

silveira.i.n@usp.br

University of São Paulo – USP

Camily Vitoria Manoel da Silva

University of São Paulo – USP

Gabriella Naser

University of São Paulo – USP

Luiza Castro Machado

University of São Paulo – USP

John Arlley Sousa Pinho de Lira

University of São Paulo – USP

Alexandro Guterres

University of São Paulo – USP

Research Article

Keywords: multi-layer integration, alternative splicing, RNA editing, differential gene expression, glioblastoma stem cells, Zika virus

Posted Date: November 23rd, 2026

DOI: https://doi.org/10.21203/rs.3.rs-11653803/v1

License: This work is licensed under a Creative Commons Attribution 4.0 International License.
Read Full License

Additional Declarations: No competing interests reported.

Beyond the Antiviral Echo: Multi-Layer Transcriptomics Reveals Splicing-Centered Remodeling of the RNA-Processing Machinery during Zika Virus Infection of Glioblastoma Stem Cells

Israel Nunes Silveira[1*], Camily Vitoria Manoel da Silva[1], Gabriella Naser[1], Luiza Castro Machado[1], John Arlley Sousa Pinho de Lira[1], Alexandro Guterres[1]

[1]Department of Genetics, Ribeirão Preto Medical School, University of São Paulo – USP, São Paulo, Brazil

Keywords: multi-layer integration; alternative splicing; RNA editing; differential gene expression; glioblastoma stem cells; Zika virus.

*Corresponding author: Israel Nunes Silveira

Department of Genetics, Ribeirão Preto Medical School, University of São Paulo – USP, São Paulo, Brazil

Av. Bandeirantes, 3900 – Monte Alegre

Ribeirão Preto, SP, 14049-900, Brazil

E-mail: silveira.i.n@usp.br; israeluoo@gmail.com

Abstract

Zika virus (ZIKV) displays selective oncolytic activity against glioblastoma stem cells (GSCs), yet standard transcriptomics centered on differential gene expression highlights generic interferon responses that fail to explain oncolytic selectivity. Through multi-layer transcriptomic integration of data from two independent experiments involving GSCs (discovery and validation), we demonstrate that ZIKV-mediated oncolysis is driven by post-transcriptional vulnerability rather than mRNA abundance changes alone. While type I interferon upregulation represented a non-discriminatory cellular alarm, alternative splicing was profoundly and reproducibly remodeled (>6,700 events across >3,000 genes with high cross-cohort event-level concordance), disproportionately targeting core spliceosomal machinery. Because GSCs are deeply addicted to precise alternative splicing to maintain stemness, this viral perturbation induces synthetic lethality. Concurrently, A-to-I RNA editing remained buffered between cohorts despite strong ADAR1upregulation, consistent with ADAR1 co-optation to restrain PKR sensing while shifting the functional death burden to splicing. Cross-layer integration identified p53 signaling as the top convergent axis (permutation $p = 0.007$). Unaltered *TP53* mRNA levels were accompanied by post-transcriptional p53 release through structural remodeling of its critical negative regulators, MDM2 and MDM4, triggering downstream pro-apoptotic effectors (PMAIP1/NOXA, DDIT3). This p53 activation operates within a dynamic tug-of-war against viral survival checkpoints, driving caspase-mediated cell death once these intracellular brakes become exhausted. We propose that ZIKV nonstructural protein 5 (NS5), which accumulates in the nucleus and binds core spliceosomal factors, serves as the candidate broker exploiting GSC spliceosome addiction. Together, our findings reframe ZIKV oncolysis around post-transcriptional RNA processing collapse, identifying splicing perturbation and p53 brake remodeling as central determinants of tumor-selective viral cytotoxicity.

1. Introduction

Glioblastoma (GBM) remains the most aggressive primary brain tumor, and its lethality rests substantially on a subpopulation of glioblastoma stem cells (GSCs) that drive recurrence, resist radio- and chemotherapy, and persist in hypoxic microenvironments (Yoshida and Saya 2016; Alves et al. 2021; Sarrazin et al. 2026). A growing body of evidence indicates that GSC identity and therapeutic plasticity are not encoded at the transcriptional level alone: alternative splicing deciphers the neurodevelopmental hierarchies of adult glioma and exposes therapeutic targets (Song et al. 2024), lineage-specific exon inclusion actively promotes GBM progression (Ferrarese et al. 2014), and aberrant splicing together with RNA-modification layers dynamically regulates glioma cell fate and drug resistance (Dome et al. 2022; Piperi et al. 2023; Ben Mrid et al. 2025). Pharmacological disruption of the spliceosome itself, for instance, SF3B1 inhibition, dismantles GBM malignancy and prolongs survival in preclinical models (Fuentes-Fayos et al. 2022), demonstrating that the post-transcriptional machinery is not a passive correlate but a functional dependency of the GSC state.

Oncolytic virotherapy with Zika virus (ZIKV) emerged from the observation that the virus preferentially infects and kills patient-derived GSCs while sparing differentiated tumor cells (Zhu et al. 2017). This paradigm has since been extended to ex vivo primary tumors, live-attenuated vaccine strains, and pediatric brain tumors (Francipane et al. 2021; Garcia et al. 2023; Victorio et al. 2024), with entry selectivity attributed to a SOX2–integrin αvβ5 axis that couples stemness to viral permissiveness (Zhu et al. 2020). Mechanistically, ZIKV has been reported to trigger apoptosis via miR-34c induction in GSCs (Iannolo et al. 2019), with interferon signaling dominating the host response, while noting that post-transcriptional layers remain essentially unaddressed (Menezes et al. 2026). Notably, the field continues to interpret ZIKV–GSC interactions almost exclusively through differential gene expression, even though the infected cells being profiled carry tumor-specific alterations in RNA processing; whether ZIKV exploits, perturbs, or exhausts this machinery to execute oncolysis remains unknown (Zhu et al. 2017).

Alternative splicing and A-to-I RNA editing constitute the two best-characterized post-transcriptional layers in glioma stem cell biology. ADAR1-mediated editing sustains GSC maintenance (Jiang et al. 2022) and, reciprocally, promotes ZIKV replication by restraining PKR activation (Zhou et al. 2019), placing the editing enzyme at the host–virus interface. In flaviviruses more broadly, editing and splicing factors such as ADAR and DDX3X segregate with proviral susceptibility modules in neural progenitors (Owaresat et al. 2026), and splicing

has been measured in only a single ZIKV-infected cell type to date, a neuroblastoma line, not GSCs (Bonenfant et al. 2020). Despite this convergence, an integrated map of expression, alternative splicing, and A-to-I editing during ZIKV infection of GSCs has never been generated, and the existing transcriptomic record cannot distinguish which layer carries information relevant to cell death rather than to generic antiviral defense.

The viral non-structural protein 5 (NS5) is the prime candidate broker of such crosstalk. NS5 is a dual-function enzyme, an N-terminal methyltransferase and a C-terminal RNA-dependent RNA polymerase, whose structure, replication function, and antagonism of type I interferon signaling are well established (Best 2017; Wang et al. 2018). Beyond interferon suppression, NS5 accumulates in the nucleus (Zhao et al. 2021), binds the core spliceosomal factor SF3B3 in ZIKV-infected cells (Chen et al. 2023), reduces SC35/SRSF2 protein levels (Li et al. 2022), and, in the related dengue virus, physically intrudes into the spliceosome to modulate host splicing (De Maio et al. 2016). NS5 is even sufficient on its own to suppress glioma cell growth *in vivo* (Li et al. 2019) and binds p53 directly, stabilizing it (Li et al. 2021). Whether ZIKV NS5 couples viral replication to the host RNA-processing machinery in GSCs, thereby converting a generic antiviral response into an oncolytic one, remains an open and testable question.

This question is anchored in a developmental logic: ZIKV preferentially infects SOX2+/PAX6+ neural progenitor cells rather than post-mitotic neurons (Li et al. 2016; Sanami et al. 2025), the same stem-state that defines GSC permissiveness. We therefore hypothesized that ZIKV infection of GSCs separates into two informational layers: a dominant but generic antiviral transcriptional program, and a splicing-remodeling program, targeting the RNA-processing machinery itself and converging on p53-linked cell-death genes, that is the more plausible carrier of oncolysis-relevant regulation, with the editing layer serving as a hijacked, pro-viral substrate. To test this, we performed a multi-layer transcriptomic analysis integrating differential expression, alternative splicing, and A-to-I editing across two independent cohorts of ZIKV-infected GSCs, distinguishing the antiviral "echo" from the post-transcriptional networks that candidate mechanisms of ZIKV-mediated oncolysis must explain.

2. Materials and Methods

2.1. Study design and data acquisition

Transcriptome data were derived from two independent, publicly available ZIKV-infection studies of patient-derived GSCs. The discovery cohort (GEO GSE102924; BioProject PRJNA399336) comprised 12 single-end RNA-seq libraries from three patient-derived GSC

lines (3565, 387 and 4121), each profiled as uninfected control and ZIKV-infected in duplicate (6 *versus* 6); the original study infected cells with the African- lineage Dakar 41519 and the Brazilian-lineage strains and harvested RNA at 48 hours post-infection, with strain assignment per library not recoverable from public metadata, so infected libraries were pooled into a single ZIKV condition. The validation cohort (SRA/ENA PRJNA473149) comprised six paired-end libraries from the GSC4121 line alone, infected at MOI 1 and harvested at 48 hours post-infection, with three mock and three infected biological replicates sequenced on the Illumina HiSeq X Ten (30.7-43.5 million read pairs, 150 bp, per library). A metadata audit against ENA and GEO sample records confirmed condition labels for all 18 libraries; an internal label-consistency audit of every analytical artifact (count matrices, rMATS b1/b2 manifests, editing aggregation dictionaries) against the official records identified and corrected a sample-label transposition in the discovery-cohort editing pipeline prior to final analyses, and all editing results were regenerated after correction (final differential-site count 290 *versus* 374 before correction; the corrected values are reported throughout).

2.2. Preprocessing and quality control

Raw reads were assessed with FastQC v0.12.1, and per-sample reports were inspected before and after filtering. Validation-cohort libraries were adapter-trimmed with fastp v0.23.4 with paired-end-aware adapter detection , quality threshold 20, and sliding-window trimming from both read ends. Discovery-cohort single-end libraries passed every FastQC module and required no trimming. Post-alignment quality control was executed with RSeQC v5.05, with read duplication and inner distance ran in parallel per library against a one-transcript-per-gene canonical GENCODE v50 bed12 (78,733 transcripts); duplication rates, proper-pair fractions, inner distance and 5'/3' gene-body ratios were consolidated per library (Supplementary Table S1). The unmapped fraction of every library was re-aligned against complete ZIKV genomes, the Dakar 41519 genome (HQ234501) for the discovery cohort, and a three-strain panel (Dakar 41519, MR766 NC_012532, Brazilian PE243 KX197192) for the validation cohort, whose strain was thereby assigned empirically, to quantify viral RNA content.

2.3. Read alignment and gene-level quantification

Reads were aligned to the GRCh38 primary assembly with HISAT2 v2.2.1 in transcript-aware mode against a shared genome_tran index built from GENCODE v50, with identical parameters across cohorts (validation: paired-end, -p 8; discovery: single-end, -p 8); sorted BAMs were produced with samtools v1.23.1. Gene-level counts were generated with

featureCounts (Subread) v2.1.1 in the appropriate library mode, -t exon -g gene_id against GENCODE v50, retaining full ENSG versioned identifiers. Mapping-rate and assignment summary tables were retained for all 18 libraries.

2.4. Differential gene expression

Genes were pre-filtered to those with at least 10 reads in at least 3 samples, and differential expression was estimated with DESeq2 v1.50.2 (R v4.5.2) using the design ~ condition, Wald test, contrast ZIKV *versus* Control, per cohort. Variance-stabilizing transformation (blind = FALSE on the fitted model) was used for sample-level scoring and visualization. Differential expression was declared at $|\log_2 FC| >= 1.5$ and Benjamini-Hochberg adjusted $p < 0.05$, and the resulting gene lists were annotated with gene symbols from GENCODE v50. No batch covariate was required within either cohort (single instrument per cohort); cross-cohort comparisons were performed exclusively at the level of replicated findings, never on raw count magnitudes.

2.5. Alternative splicing analysis

Alternative splicing was quantified with rMATS v4.3.0 with variable read length handling (150 for the validation cohort and 50 for the discovery cohort), paired and single-end modes respectively, against GENCODE v50, with mock/ control as b1 and ZIKV as b2 in both cohorts; junction-counts-with-exon-bodies (JCEC) estimates were used as the primary analysis and JC estimates retained as sensitivity. Significant events were defined at FDR < 0.05 (IncLevelDifference reported as DeltaPSI, positive meaning higher inclusion in ZIKV after the b1/b2 orientation is accounted for). Cross-cohort event matching was performed by coordinate signature - event type, chromosome, strand and all splice-junction coordinates - rather than by rMATS event identifiers, which are run-specific ordinals; events significant in both cohorts were termed replicated, and direction concordance was tested with a sign test (binomial) plus Spearman correlation of DeltaPSI between cohorts.

2.6. A-to-I RNA editing analysis

A-to-I editing was detected per cohort with samtools mpileup-based calling in REDItools style: candidate A-to-G sites were required to have coverage >= 10, editing frequency between 0.10 and 0.95, at least 2 supporting G reads, base quality >= 25 and mapping quality >= 20, and to pass a Fisher- based strand-bias filter ($p >= 0.05$) computed from forward/reverse support. Sites were aggregated across samples of a cohort when detected in at

least 2 samples, and differential editing was declared at |delta frequency| > 0.10 between condition means. The discovery-cohort editing analysis was regenerated after the label-correction described in 1.1, and the corrected aggregates are reported. Cross-cohort site matching used chromosome and position (hg38); replication of differential editing was tested with the hypergeometric overlap test against the universe of aggregated sites, and background-editome conservation was quantified as the fraction of discovery aggregated sites recovered in validation (and, restrictively, within the shared GSC4121 line). Sites were annotated to genomic regions (CDS, UTR, intron, intergenic) from GENCODE v50 with CDS priority; recoding consequences were derived by codon reconstruction from transcript-level CDS annotation in transcript orientation, applying the A→G change and translating before and after, with antisense-in-CDS events excluded from the recoding category.

2.7. Functional enrichment analysis

Functional enrichment was performed independently for each analytical layer and cohort. Over-representation analysis was conducted with Enrichr-backed gseapy against Gene Ontology Biological Process 2026, KEGG 2026 Human, Reactome 2024 and WikiPathways 2024 Human, using as background the set of tested genes of the corresponding layer and Benjamini-Hochberg adjustment, applied separately to induced and repressed differentially expressed genes (DEGs) and to the gene sets underlying significant splicing and differential editing. Gene set enrichment analysis was performed with GSEA in pre-ranked mode, applied independently to each cohort, on all expressed genes ranked by the DESeq2 Wald statistic (sign x significance). Sample-level pathway activity was scored with ssGSEA (gseapy) on variance-stabilized counts for the Hallmark Interferon-alpha, Interferon-gamma and p53 pathways and the Reactome TP53-transcriptional-regulation set, tested between conditions with exact Mann-Whitney (Wilcoxon) tests; the minimum attainable exact p at 3-*versus*-3 (0.10) is reported where applicable. The analysis environment comprised Python 3.12.3 with gseapy 1.3.1, pandas 2.3.3, numpy 2.4.6 and scipy 1.18.0, and R 4.5.2 with DESeq2 1.50.2.

2.8. Multi-layer integration

Genes implicated across layers were compared by intersection per cohort with the universe of DESeq2-tested genes as background, and pairwise overlaps were tested for enrichment or depletion with the hypergeometric test. Directional concordance between layers was assessed by linking DEG $\log_2$FC sign to the majority splicing direction per gene (mixed-direction genes reported separately) and testing foreground concordance against a 50% null

with a one-sample binomial test, with Spearman correlation of log_2FC and gene-level median DeltaPSI as effect-size association. Pathway-level convergence was evaluated over curated pathway collections (MSigDB Hallmark, Reactome, KEGG) as the fraction of pathway genes affected in at least two of the three layers, tested against 1,000 gene-set-size-matched random permutations with Benjamini-Hochberg adjustment; union-level over-representation was computed for the union of all layer gene sets. Cross-layer emergent signals were explored with a combined-rank GSEA and are reported only when supported by the permutation analysis.

2.9. Detection of host-viral chimeric transcripts.

To search for host-ZIKV chimeric RNAs, the six paired-end validation libraries were re-aligned with STAR 2.7.11b against a combined index of the GRCh38 primary assembly (GENCODE v50 annotation) and three complete ZIKV genomes (Dakar 41519/HQ234501, MR766/NC_012532, PE243/KX197192; sjdbOverhang 149). Chimeric detection used --chimSegmentMin 15 --chimJunctionOverhangMin 15 with --outFilterMultimapNmax 5; junctions were filtered to ≥3 uniquely mapped supporting reads, with the three mock libraries processed identically as background controls. Junction mechanism was classified from ±25 nt of reference sequence flanking each breakpoint: GT-AG dinucleotides bracketing the junction (spliceosome-mediated trans-splicing), 4-10 nt microhomology shared across the breakpoint (viral RNA-dependent-RNA-polymerase template switching), or blunt ligation. For cross-cohort replication in the single-end 50-bp discovery libraries, where de novo chimera calling is not feasible, junction-spanning 25-nt k-mers (13,008 k-mers from 813 validated junctions, each crossing a breakpoint and therefore absent from both parental genomes) were searched across all 383 million discovery reads; a junction was called replicated with ≥2 supporting reads in infected libraries and ≤1 in any mock.

To assess the theoretical translatability of chimeric transcripts, each junction's ±120/150-nt reference sequence was scanned for host-derived upstream AUG codons opening reading frames that traverse the breakpoint without an intervening stop codon (minimum eight codons), following the hybrid-gene model (Ho et al. 2020); junction-spanning ORF counts were benchmarked against 813 (and 1,626 supplementary) size-matched simulated junctions joining random human and viral coordinates, which showed no enrichment of crossing ORFs at any length threshold, reported as presence, not enrichment.

2.10. Statistics and reproducibility

All thresholds, per-layer sample counts and censoring rules are as declared above; per-contrast counts and FDR tables are provided in the released sidecar TSV files. Multiple testing within each analysis used Benjamini-Hochberg FDR, with significance at FDR < 0.05 unless stated (GSEA prerank reporting at FDR < 0.25 following convention). Exact tests were preferred at small *n* (binomial, Mann-Whitney, hypergeometric), and the combinatorial floor of exact p-values at 3-*versus*-3 designs is declared where it bounds interpretation. All pipelines were executed using version-controlled shell and Python scripts, with logs retained for each step. Intermediate and final result tables are available in the Supplementary Files.

3. Results

3.1. Sequencing quality, read filtering, and alignment

The 12 single-end libraries of the discovery cohort, containing 25.5 – 36.1 million 50-bp reads each, were assessed for quality with FastQC and approved in every module, so no trimming step was required before alignment. The six paired-end libraries of the validation cohort (61.4 – 87.0 million read pairs each) were adapter-trimmed with fastp, which retained 95.0 – 97.1% of reads and raised mean Q30 content from 87.4 – 88.8% to 90.0 – 90.6%; FastQC re-inspection after filtering returned all modules in the pass range for every library.

Alignment against the same transcript-aware GRCh38 index (HISAT2 2.2.1) mapped 96.6 – 98.6% of reads in the six discovery control libraries and 80.9 – 82.3% of read pairs in the three validation mock libraries, but only 65.5 – 79.6% in the six discovery infected libraries (a reduction of 17 – 32 percentage points against line-matched controls) and 45.5 – 54.1% in the three validation infected libraries (27 – 36 points against the mock mean), in both cohorts the reduction was confined to infected libraries and tracked infection status rather than sequencing depth (Figure 1A).

Re-alignment of the unmapped fraction against complete ZIKV genomes traced this reduction to viral RNA in the discovery cohort but not in validation. In discovery, 8.6 – 19.5% of all reads in infected libraries mapped to the ZIKV Dakar 41519 genome (HQ234501) *versus* 0.03 – 0.05% in controls, accounting for roughly half of the alignment-rate reduction (45 – 61% across line-matched pairs), with the most permissive line, GSC4121, carrying the highest viral fraction (16.4 – 19.5%). In validation, alignment against a three-strain panel (African Dakar 41519 and MR766; Brazilian PE243) assigned the infection unambiguously to a Brazilian/Asian-lineage strain, infected reads mapped exclusively to PE243, yet recovered only 0.027 – 0.030% viral read pairs (mock libraries: none detected). The infected-specific reduction

in this cohort was therefore not attributable to viral reads; its unmapped fraction showed no fragmentation (median read length 150 bp, unchanged), no ribosomal RNA enrichment (0.2 – 0.8% against 45S/5S rRNA) and no low-complexity excess, with a modest GC shift (56.9% in mock to 59.5 – 60.5% in infected) as the only detectable deviation.

Re-alignment of the validation cohort against a combined human-ZIKV index with chimeric detection identified host-viral chimeric junctions as one quantifiable component of this landscape: infected libraries contained 813 distinct human-ZIKV junctions (≥3 uniquely mapped reads each; 59 – 94 per million uniquely mapped reads) whereas no mock library yielded any junction above background. Chimeric reads nevertheless account for a small fraction of the residual, whose dominant composition remains unresolved and is reported as a limitation; the two cohorts consequently replicate the infected-specific alignment reduction through partially distinct read populations (viral reads in discovery; chimeric and unresolved fractions in validation). Junction-spanning open reading frames are present in most chimeras (713 of 813, median 46 codons), at frequencies indistinguishable from size-matched simulated junctions, establishing that junction peptides are structurally possible without claiming selection for translatability.

Alignment quality metrics completed this picture. Mean duplication rates were 49.8 – 63.0% in discovery (lower in infected libraries: 49.8 – 59.8% *versus* 56.9 – 63.0% in controls) and 58.8 – 66.0% in validation, within the range expected for deeply sequenced RNA libraries. Properly paired reads in the validation cohort spanned 64.6 – 67.1% of mock pairs but only 34.8 – 43.3% of infected pairs, and median inner distance was -32 to -19 bp (short inserts with read overlap); single-end discovery libraries carry no pair metrics by design. Gene-body coverage was modestly 5'-biased in both cohorts (5'/3' ratios 1.39 – 1.58 discovery, 1.15 – 1.24 validation), slightly stronger in infected discovery libraries (1.52 – 1.58 *versus* 1.39 – 1.47 in controls), indicating partial 3' truncation of transcripts that did not preclude quantification. Taken together, the two cohorts were sequenced and aligned to equivalent standards, with the alignment-rate reduction of infected libraries explained by viral RNA content in the discovery cohort and quantified as an unresolved non-viral residual in validation; cross-condition comparisons throughout this work rely on the mapped human fraction, which remained depth-sufficient in every library. No sample was excluded on quality grounds.

3.2. Global transcriptional response to ZIKV infection

Differential expression analysis of the discovery cohort identified 1,512 genes with significant changes upon infection (1,216 induced, 296 repressed; $|\log2FC| \geq 1.5$, padj < 0.05) (Figure 1B). The response was dominated by induction of antiviral and inflammatory effectors: the chemokine *CXCL8* (IL-8, +9.72) and *IFNB1* (+9.42) were the most induced genes genome-wide, followed by *CXCL3* (+9.12), *IFNL1* (+9.07), *BCO1* (+8.76), *CCL5* (+8.75), *CXCL10* (+8.75) *GBP4* (+8.75) and the IFN-stimulated effectors *OASL* (+8.73), *MX2* (+6.97), *IFIH1* (+6.84) and *IFIT1* (+6.75); the induced set also included non-coding transcripts coupled to the antiviral response, such as *CCL5-AS1* (+7.03), the miR-34 host gene *MIR34AHG* (+3.68) and *MIR22HG* (+3.54) (Figure 1C).

Beyond the threshold-defined DEG set, a broader padj-significant, sub-threshold tier (padj < 0.05, $|\log_2FC| < 1.5$) carried the cell-death regulatory machinery: the anti-apoptotic module *BIRC3* (+7.31) and *TNFAIP3* (+5.51) exceeded the threshold, whereas *MCL1* (+0.77, padj = 1.5×10^{-6}), *XIAP* (+0.24, padj = 6×10^{-3}), *CASP3* (+0.93, padj = 4.5×10^{-35}) and *CASP7* (+0.97, padj = 4.4×10^{-24}) were padj-significant below it, alongside threshold-exceeding pro-death mediators (*FAS* +2.40, *CASP1* +3.20), documenting a dual pro- and anti-apoptotic configuration of the response at the expression level, the classic signature of TNF/NF-κB-centered signaling carrying both arms of the death decision. In contrast, stem-cell state markers were consistently but modestly repressed (*SOX2* -1.04, *NES* -1.17, *MYC* -1.19, *EGFR* -0.97; all padj < 10^{-24} yet below the differential-expression threshold), indicating that infection reshaped the antiviral program without abolishing the GSC identity signature (Supplementary Figure 1).

Enrichment analysis of the discovery cohort characterized the infected transcriptome at the pathway level. Over-representation analysis of the 1,216 induced genes against four curated databases returned 873 significant terms (GO Biological Process 454, KEGG 119, Reactome 117, WikiPathways 183; FDR < 0.05), dominated by antiviral and inflammatory programs: defense response to virus (GO:0051607, 50/198 genes, FDR = 3.3×10^{-29}), interferon alpha-beta signaling (Reactome R-HSA-909733, 33/78, FDR = 1.7×10^{-27}), TNF signaling (KEGG, 33/118, FDR = 5.1×10^{-21}) and cytokine-cytokine receptor interaction (WikiPathways WP5473, 39/255, FDR = 5.4×10^{-15}) (Figure 2A). To capture coordinated shifts below the significance threshold, we re-ranked all expressed genes by the DESeq2 Wald statistic and ran pre-ranked GSEA: NF-κB signaling (Normalized Enrichment Score (NES) +2.60) and TNF signaling (+2.55) led the induced pole, with convergent antiviral signals across databases, defense response to virus (GO, +2.64), interferon alpha/beta signaling (Reactome, +2.98), type II

interferon signaling (WikiPathways, +2.63) and RIG-I-like receptor signaling (KEGG, +2.24), whereas translation dominated the repressed pole (cytoplasmic translation GO:0002181, -2.59; KEGG ribosome, NES -2.88; all FDR < 0.001), indicating a genome-wide shutdown of the translational machinery accompanying the antiviral program (Figure 2B). Repressed-gene over-representation returned 23 significant terms across the four databases (GO 15, KEGG 0, Reactome 7, WikiPathways 1), led by potassium ion transport (8/127, FDR = 6.2 x 10^{-4}), metal ion transport (9/180, FDR 6.2 x 10^{-4}), chemical synaptic transmission (9/260, FDR = 6.1 x 10^{-3}), neuronal system (13/411, FDR = 3.8 x 10^{-4}) and transmission across chemical synapses (9/269, FDR = 2.9 x 10^{-3}). No cell-death term reached significance among repressed genes. Thus, 873 terms were associated with induced genes versus 23 with repressed genes.

The stress-response arm of this program warranted inspection at the gene level, because its canonical regulators are controlled post-transcriptionally rather than transcriptionally. The integrated stress response/unfolded protein response (ISR/UPR) effector genes were induced: *DDIT3* (*CHOP*, +2.62, padj = 3×10^{-128}), *HSPA5* (BiP, +1.60, padj = 3×10^{-106}), exceeded the significance threshold, whereas *ASNS* (+1.13), the ER-stress sensor ERN1 (*IRE1*, +0.93), *XBP1* (+0.63) and *ATF6* (+0.41) were padj-significant in the sub-threshold tier. Yet *ATF4*, the transcription factor upstream of DDIT3, declined at the mRNA level (-0.87, padj = 1×10^{-28}), the expected behavior of a gene regulated at the level of translation (uORF-mediated, downstream of phosphorylated eIF2α), and neither the upstream kinase EIF2AK2 (*PKR*, -0.08) nor the alpha subunit EIF2S1 (*eIF2α*, -0.10) changed in transcript abundance. Read together with the ribosomal shutdown of the preranked GSEA, this pattern is consistent with an ISR engaged post-transcriptionally: effectors induced, transcriptional regulators flat or declining, and translation globally repressed.

The validation cohort reproduced this architecture with 355 DEGs (344 induced, 11 repressed), of which 198 induced genes (58%) were shared with the discovery cohort. Induction of the antiviral axis was concordant in magnitude and direction (*CCL5* +9.80, *IFNB1* +9.57, *OASL* +7.28, *IFIT1* +5.43, *IFIH1* +4.38), as was the modest repression of stem markers (*SOX2* -0.39, *NES* -0.50, *MYC* -0.51). Pathway-level concordance exceeded gene-level concordance. Of the gene-ontology and pathway terms significantly enriched among induced genes in the discovery cohort, 15 - 27% were also significant in the validation cohort depending on the database (hypergeometric $p \leq 5.9 \times 10^{-11}$ across all four), with "defense response to virus" (GO:0051607; FDR 3.3×10^{-29} and 6.8×10^{-17}) and "interferon alpha-beta signaling" (Reactome R-HSA-909733; FDR 1.7×10^{-27} and 5.6×10^{-24}) as the top shared terms in both.

A threshold-free pre-ranked GSEA of the validation cohort (Wald-statistic ranking) reproduced both poles: Defense response to virus (+2.79), TNF (+2.37), NF-κB (+2.25), RIG-I-like receptor signaling (+2.12) and interferon alpha-beta (+2.83) signaling led the induced extreme (all FDR < 0.001), whereas the translational shutdown deepened (KEGG ribosome NES -3.00; rRNA processing -2.97; spliceosome -2.58), extending the repressed pole from translation to ribosome biogenesis and splicing machinery (Figure 2C). Per-sample scoring confirmed the program at the sample level: ssGSEA enrichment scores for interferon-alpha and interferon-gamma responses increased in every infected library relative to every control in both cohorts (discovery $p = 0.0022$; validation $p = 0.10$, the minimum attainable at $n = 3$ per group), establishing a conserved, direction-consistent antiviral transcriptional program as the dominant expression-level response to ZIKV in GSCs.

3.3. Alternative splicing remodeling upon ZIKV infection

The rMATS identified 6,749 significant splicing changes (FDR < 0.05) across 3,036 genes in the discovery cohort, spanning twice as many genes as the differential expression layer. Skipped exon (SE) was the largest class (3,028 events), followed by retained introns (RI, 1,178), alternative 5' splice sites (A5SS, 962), mutually exclusive exons (MXE, 828) and alternative 3' splice sites (A3SS, 753). Events were directionally skewed toward exon skipping and splice-site switching rather than inclusion: skipping exceeded inclusion among SE events (1,741 *vs* 1,286), 72% of A5SS events shifted away from the annotated 5' site, and RI were more often lost than gained in the infected state (691 *vs* 487), a pattern consistent with reduced spliceosome fidelity upon infection (Figure 3A).

The event burden was strongly concentrated in a subset of genes. *HNRNPC*, encoding a core heterogeneous nuclear ribonucleoprotein, was the most affected gene genome-wide with 45 significant events (mean dPSI -0.176), followed by *WARS1* (38), the small nucleolar RNA host gene *SNHG17* (36), *PFDN5* (30), *GAS5* (28), *RANGAP1* (25) and *ANXA2*, *DDX5*, *SRSF7* and *EEF1D* (23 events each). The list was dominated by two functional groups: components of the RNA-processing machinery itself (H*NRNPC, DDX5, SRSF7, SNHG17, GAS5*) and genes coupling transcription to translation (*EEF1D, WARS1, PFDN5*), indicating that infection remodels the regulators of the very process being disrupted. Event burden and effect size were partly decoupled: among genes with few but individually large-magnitude changes, *MDM2* carried a potent exon-inclusion event (dPSI +0.46, FDR = 3×10^{-13}) whose cross-cohort replication is examined in Section 4. Beyond protein-coding targets, snoRNA host genes were

consistently among the most remodeled transcripts, with *SNHG17* significant in both cohorts (36 and 14 events, concordant direction) alongside *SNHG1*, *SNHG5*, *ZFAS1* and *SNHG12*, 30 non-coding hosts carried significant events in both cohorts, two-thirds of them directionally concordant (Figura 3B).

Over-representation analysis of the 3,036 genes with altered splicing returned broad enrichment of RNA- and protein-metabolism programs (Reactome 603, GO 543, KEGG 115 and WikiPathways 161 significant terms; FDR < 0.05). Figure 3C summarizes this landscape using the top three terms per database plus three prespecified p53/cell-death terms: Reactome metabolism of proteins (451/2,067; FDR = 1.8×10^{-36}), metabolism of RNA (220/761; 5.3×10^{-34}) and cellular responses to stimuli (223/887; 4.6×10^{-25}); GO RNA processing (107/291; 5.0×10^{-24}), regulation of translation (79/201; 1.5×10^{-19}) and gene expression (113/381; 3.7×10^{-17}); KEGG protein processing in the endoplasmic reticulum (61/171; 4.2×10^{-13}), amyotrophic lateral sclerosis (96/362; 7.8×10^{-12}) and Parkinson disease (75/263; 6.3×10^{-11}); and WikiPathways mRNA processing (57/125; 1.0×10^{-17}), VEGFA-VEGFR2 signaling (115/430; 2.6×10^{-14}) and cytoplasmic ribosomal proteins (35/88; 1.1×10^{-8}). Within this landscape, the prespecified cell-death terms were prominently enriched: transcriptional regulation by TP53 (Reactome R-HSA-3700989; 96/362; FDR = 4.1×10^{-12}), programmed cell death (R-HSA-5357801; 50/202; 9.2×10^{-6}) and KEGG apoptosis (40/136; 1.7×10^{-6}), establishing p53-linked cell-death genes as a preferential target of infection-associated splicing remodeling.

The validation cohort independently reproduced scale, targets and program: 5,688 significant events across 2,917 genes with the same event-type ranking (SE 2,652 > RI 996 > A5SS 704 > A3SS 683 > MXE 653) and the same skipping-biased direction (Figure 3A). Six of the ten most event-dense genes in the discovery cohort reappeared among the most affected in validation (*HNRNPC* remained the top gene with 71 events, followed by shared *WARS1*, *SNHG17*, *PFDN5*, *GAS5* and *EEF1D*), joined by *AKAP8L*, ranked 15th in discovery but among the top of validation, and 1,356 genes (44.7% of the discovery set) were splice-altered in both cohorts (hypergeometric $p \approx 0$) (Figure 3B). The cell-death program was again enriched among splice-altered genes (transcriptional regulation by TP53, FDR = 1.6×10^{-4}; programmed cell death, 3.4×10^{-2}; KEGG apoptosis, 3.8×10^{-2}), and pathway-level concordance ranged from 12% to 33% of significant terms across databases, confirming splicing remodeling as a reproducible feature of ZIKV infection in GSCs and setting the stage for the event-level analysis of Section 3.4.

3.4. Event-level replication of splicing changes across cohorts

Gene-level and pathway-level concordance left open whether the same individual splicing events recur across cohorts. Because rMATS event identifiers are assigned per run, they cannot be compared directly between datasets; we therefore paired events by their full coordinate signature (event type, chromosome, strand and all splice junction coordinates), which recovers 1,063 events significant in both cohorts (FDR < 0.05 each) *versus* only 117 recovered by naive identifier matching, a nine-fold difference confirming that coordinate-based pairing is required for cross-run comparison.

Across these 1,063 replicated events, the direction of PSI change was concordant in 95.9% (1,019/1,063; binomial $p = 4.7\times10^{-242}$) and effect sizes correlated strongly between cohorts (Spearman $\rho = 0.795$, $p = 9.1\times10^{-233}$) (Figure 4A). Concordance was uniformly high across event classes, SE 97.3%, A5SS 96.8%, MXE 96.2%, A3SS 94.9% and RI 92.6%, and the replicated events mapped to 617 distinct genes (Figure 4B). When an event is significant in both cohorts, then, its direction is essentially determined, establishing a layer of splicing regulation that survives changes in cell-line composition (three lines *versus* one), library layout (single- *versus* paired-end), depth and infection protocol.

The strongest replicated events illustrate the range of effect sizes. The *MDM2* exon at chr12:68816811-68816945, flagged in Section 3, showed increased inclusion upon infection in both cohorts (discovery ΔPSI +0.46, FDR = 3×10^{-13}; validation ΔPSI +0.065, FDR = 9×10^{-6}), with the attenuated validation magnitude consistent with the reduced statistical power of three replicates per group (Figure 4C). This exon is coding and lies wholly within the N-terminal p53-binding domain of MDM2 (amino acids 53 – 96 of the reference isoform). *HNRNPC*, the most event-dense gene in both cohorts, carried a concordant A5SS event (ΔPSI -0.309 and -0.089). Beyond these anchor cases, most concordant genes were hit by different specific events in each cohort: gene-level convergence without event-level identity, indicating that infection directs its splicing program at the level of target genes rather than individual splice junctions, with a core of ~1,000 junction-level changes robust enough to recur under independent experimental conditions.

3.5. A-to-I RNA editing: a stable background editome without reproducible differential editing

RNA editing was quantified with REDItools3 restricted to A-to-G calls and filtered against common germline variants (dbSNP b151). The discovery cohort yielded 838

reproducible A-to-I sites (aggregated across samples with coverage ≥ 10, editing frequency 0.10 – 0.95, and at least two supporting reads per site), 138 of them differentially edited between control and infected conditions; the deeper, paired-end validation cohort yielded 7,162 sites and 1,665 differential ones. Despite the eight-fold difference in detection, the background editome was conserved across cohorts: 68.5% of the discovery aggregated sites were recovered in the validation cohort, and editing frequencies at shared sites were near-identical between the two independent calling runs of this work (Pearson r = 0.989 – 0.993 in the cross-implementation benchmark) (Figure 5A). The editing machinery itself responded to infection: *ADAR1* (HGNC symbol ADAR; encoding the predominant p110/p150 deaminase) was induced in the padj-significant, sub-threshold tier ($\log_2$FC +0.68, padj = 1.1×10^{-24} discovery; +0.34, padj = 9.2×10^{-7} validation), while its paralogue *ADARB1* (encoding ADAR2) declined in the discovery cohort (-0.39, padj = 1.0×10^{-4}) and was unchanged in validation, a divergent repositioning of the two principal editing enzymes that matches their distinct substrate repertoires.

Differential sites were predominantly located in regulatory regions: 68 – 75% UTRs and 6 – 25% CDS (Figure 5B). Codon-level inspection of all CDS sites on positive-strand genes (84) identified 54 missense editing candidates surviving common-variant exclusion, including two recurring at identical coordinates in both cohorts (*SH2B1* N→S at 16:28871920 and *CDK13* Q→R at 7:39950949) and, in validation, candidates in infection-coupled genes (*IFNAR1* T→A, *TARDBP* R→G, *TET2* H→R) and cell-cycle genes in discovery (*CDK13, CDK9* M→V, *KMT2E* I→M), a set awaiting DNA-level confirmation before any functional claim. Within regulatory editing, the validation cohort placed four differential sites in cell-death executor genes (three in *APAF1*, one in *CASP9*, the latter within coding sequence), hypothesis-generating by the single-line 3v3 setting.

Differential editing did not replicate beyond chance. The overlap was 21.7% of the discovery set (hypergeometric p = 0.61), and although 73.2% of discovery differential sites remained edited at the aggregated level in validation, direction agreed in only 24 of 30 evaluable replicated sites (Figure 5C). The editing layer thus contrasts sharply with the splicing layer: a conserved background editome with induced ADAR and a filtered set of recoding candidates, but no reproducible site-level differential response.

3.6. Host-viral chimeric transcripts generated by polymerase template switching

Beyond remodelling host RNA processing, infection generates hybrid host–viral transcripts. Chimeric-aware re-alignment of the validation cohort against a combined human and ZIKV reference (three complete genomes: Dakar 41519, MR766 and the infecting PE243 strain) recovered 949 human-ZIKV chimeric junctions supported by at least three uniquely mapped reads, 813 distinct junctions, distributed across all three infected libraries (59–94 junction reads per million uniquely mapped reads), while the three mock libraries processed identically yielded none above background. The junction landscape was dominated by the structural rather than protein-coding regions of the host partners, spread uniformly across the viral genome without 5′-end concentration (excluding a cap-snatching mechanism), and was not attributable to single recurrent artifacts: the ten most-supported junctions carried 6.8% of the total signal.

The breakpoint architecture identified the generating mechanism. Of the 949 junctions, 723 (76%) showed four-to-ten-nucleotide microhomology between the two parental sequences at the junction, the canonical template-switching signature of viral RNA-dependent RNA polymerases, whereas spliceosome-mediated trans-splicing was excluded (seven GT-AG junctions, 0.7%, at the frequency expected by chance) and blunt ligation accounted for the remainder. Cross-cohort replication was tested by targeted search of 13,008 junction-spanning 25-mers (each present in neither parental genome) across the 383 million single-end reads of the discovery cohort, where de novo chimera detection is not feasible: infected libraries carried a 6.3-fold excess of junction-spanning reads over mocks, and seven specific junctions replicated under the strictest criterion (≥2 supporting reads in infected libraries, ≤1 in any mock). Host–ZIKV chimeric transcripts therefore arise reproducibly across cohorts, strains and cell-line compositions, as a by-product of the copying promiscuity of the viral polymerase rather than of host splicing machinery.

3.7. A transcriptional signature consistent with p53 pathway activation

Sections 3.3 and 3.4 established the p53-linked cell-death program as a preferred target of infection-associated splicing remodeling. To quantify this axis at the expression level, we scored each library of the discovery cohort against curated p53 gene sets. Per-sample enrichment of the Hallmark p53 pathway increased upon infection in every infected library relative to every control (mean difference +765 enrichment units, exact Wilcoxon $p = 0.0022$, the value attained by perfect 6-*versus*-6 separation; Figure 6), and the Reactome set of TP53-regulated transcription rose in parallel (+91, $p = 0.0043$); ranking all expressed genes by fold-

change reproduced the result without any significance threshold (KEGG p53 signaling, NES +1.71, FDR = 0.01). The canonical transactivation targets followed the same pattern with large effect sizes: *PMAIP1* (NOXA) was induced 13.5-fold at the mRNA level (log_2FC +3.75, padj = 3×10^{-153}), *MDM2* 2.4-fold (+1.24, padj = 8×10^{-69}) and *CDKN1A* (p21) 2.3-fold (+1.23, padj = 6×10^{-14}), whereas *TP53* mRNA itself remained unchanged (+0.06, not significant). This combination constitutes a transcriptional signature consistent with post-translational stabilization of pre-existing p53 protein rather than with increased *TP53* transcription. Notably, two core components of the intrinsic, mitochondrial apoptotic pathway declined at the mRNA level (*BAX* -0.36, padj = 5.6×10^{-6}; *CYCS* -0.40, padj = 5.6×10^{-8}), arguing against a simple transcriptional-activation model of the intrinsic pathway and indicating that if mitochondrial apoptosis executes downstream of p53 in this system, it is engaged post-transcriptionally. The signature emerged in a specific cellular context: the same infected libraries showed only modest repression of stem-cell markers (*SOX2* -1.04, *NES* -1.17, *MYC* -1.19; Section 2), so p53 target induction and erosion of the GSC identity program were concomitant rather than sequential features of the infected state.

The two canonical negative regulators of p53 integrated the expression and splicing layers in complementary ways. MDM2, the RING-finger E3 ligase that targets p53 for degradation, was the only p53-axis gene significantly altered in both layers: induced at the mRNA level (+1.24) and remodelled at the transcript-structure level, carrying the replicated exon-inclusion event at chr12:68816811-68816945 (dPSI +0.46, FDR = 3×10^{-13} in discovery; directionally replicated in validation, Section 4) in addition to a mutually exclusive exon switch (dPSI -0.24, FDR = 1×10^{-7}) and two weaker skipping events. Its paralog and heterodimerization partner *MDM4* showed the mirror configuration, altered only in the splicing layer, with two exon-inclusion events (dPSI +0.42 and +0.32, FDR < 1×10^{-4}) and no significant expression change. In the absence of protein or isoform-resolved data, these observations establish a multi-layer convergence of infection on both principal inhibitors of p53, one hit at both mRNA abundance and transcript architecture, the other at transcript architecture alone, while the functional consequence of each individual event is left for the Discussion.

The validation cohort reproduced the direction of every component of the axis within the limits of its statistical power. Hallmark p53 enrichment rose in all three infected libraries (mean +387, exact $p = 0.10$, the minimum attainable at three replicates per group), *CDKN1A* remained significantly induced (+0.17, padj = 0.04), and the threshold-free KEGG ranking showed the same positive trend (NES +1.30, FDR = 0.26), whereas *MDM2* mRNA induction

attenuated below significance (+0.09) even as its splicing event remained significant at the coordinate level. The Reactome *TP53* set moved in the opposite direction (-53, $p = 0.10$); given the extensive gene overlap between the two p53 sets and the incompleteness of 3-*versus*-3 testing, we interpret this single reversal as inconclusive rather than as evidence against the axis. Taken together, the p53 signature was direction-consistent across cohorts, formally significant in the 6-*versus*-6 discovery setting, underpowered but never significantly reversed in validation, making it, alongside the interferon program, the most reproducible transcriptional feature of ZIKV infection in GSCs. Whether this axis also represents the dominant point of convergence across the three regulatory layers was tested next.

To place p53 activation in the context of other infection-associated programs, we extended the per-sample ssGSEA analysis to six prespecified axes in the discovery cohort. Beyond p53 and IFN-α, ZIKV increased TNF/NF-κB signaling, repressed E2F/cell-cycle and ribosome/translation programs, and lowered the GSC/stemness marker score (Figure 6); all BH $q < 0.05$). All six axes changed in the same direction in the validation cohort, although the 3-versus-3 comparison was underpowered (exact $p = 0.10$, the minimum attainable). Thus, p53 activation occurred within a coordinated multi-program state rather than in isolation. Whether this axis also represents the dominant point of convergence across the three regulatory layers was tested next.

3.8. Multi-layer convergence upon infection

Having characterized each regulatory layer independently, we quantified how often infection converged on the same genes across layers. Joining the three layers by gene identifier in the discovery cohort yielded 114 genes shared between differential expression and altered splicing (DEG ∩ SPL), 31 between altered splicing and differential editing (SPL ∩ EDI) and only 2 between differential expression and differential editing (DEG ∩ EDI); no gene was altered in all three layers. Benchmarked against chance expectation from the universe of tested genes, these intersections departed from neutrality in a structured way: DEG ∩ SPL and DEG ∩ EDI were significantly depleted relative to chance (114 observed *vs* 260 expected, 0.44-fold, $p = 3.3\times10^{-30}$; 2 *vs* 8.9, 0.22-fold, $p = 5.1\times10^{-3}$), whereas SPL ∩ EDI was the only enriched pair (31 *vs* 17.7, 1.75-fold, $p = 8.9\times10^{-4}$). The validation cohort reproduced the architecture and its significance structure at its own scale (44, 138 and 3 pairwise overlaps; DEG ∩ SPL depleted 0.66-fold, $p = 7.4\times10^{-4}$; DEG ∩ EDI 0.28-fold, $p = 5.8\times10^{-3}$; SPL ∩ EDI enriched 1.62-fold, $p = 1.1\times10^{-9}$; 1 gene, below the ~2 expected, in the triple intersection). Genes therefore tended

to be regulated by one class of mechanism rather than several, a transcriptional module (induced antiviral effectors) operating largely disjoint from a cohesive post-transcriptional module (splice-altered and differentially edited genes), while the filtering constraints of each assay and the very different layer sizes (1,512 differentially expressed genes, 3,036 splice-altered genes, 103 – 455 editing genes; 138 and 1,665 differential sites mapping to 103 and 455 genes respectively, since multiple sites can fall within one gene) set the scale of each comparison. The consistent message is complementarity, the splicing layer reaches roughly twice as many genes as the expression layer, and each layer covers territory the others do not.

The convergence that occurred was at the level of programs, not of directional signals within individual genes. Among the 114 genes that were both differentially expressed and splice-altered in the discovery cohort, the direction of the expression change agreed with the majority direction of the splicing changes in 51.5% of evaluable genes (53/103 after excluding 11 genes with mixed splicing direction; one-sided binomial $p = 0.42$), and effect sizes were uncorrelated between layers (Spearman $\rho = -0.15$, $p = 0.11$); the validation cohort gave the same null answer (47.6% concordance, $p = 0.68$; $\rho = -0.12$, $p = 0.45$). At the event level, the direction of an individual splicing event matched the expression direction of its gene at chance frequency (50.5% discovery, 33.7% validation), and the rare triple-hit genes (one in the validation cohort, none in discovery) were directionally discordant where evaluable. Within a given gene, then, the machinery of transcriptional induction and the machinery of transcript remodeling responded to infection on near-independent axes, the antiviral program being carried primarily by expression changes and the p53-linked and RNA-processing programs primarily by splicing changes, a decoupling that any mechanistic account of ZIKV oncolysis must accommodate.

To test convergence where it should matter, at the level of pathways, we scored every curated pathway for the fraction of its genes affected in at least two of the three layers, defining each layer as significant DEGs, FDR-significant splicing-altered genes, or canonical differential RNA-editing genes present in the DEG universe. Significance was assessed against 1,000 gene-set-size-matched random permutations with Benjamini-Hochberg correction. In the discovery cohort, 48 pathways passed correction, led by inflammatory and immune-presentation programs (TNFR1-induced NF-κB signaling, 19.2% of genes hit in at least two layers; antigen processing and MHC-I assembly, 18.5%; interferon-alpha response, 14.1%); KEGG p53 signaling (7.4%, BH = 0.028) and the MSigDB p53 Pathway (3.9%, BH = 0.028) were also significant, so the p53 axis of Section 6 is formally convergent in discovery but not

the leading convergent program. In validation, no pathway survived cohort-level correction (best nominal $p = 0.001$, BH = 0.10 at 3-versus-3 power; the leading candidates were NF-κB signaling 9.7%, interferon alpha/beta signaling 11.5% and the ATF4/PERK arm of the unfolded protein response 16.1-19.2%), a power limitation stated explicitly rather than interpreted as absence of convergence. The convergent programs shared conceptually across cohorts thus centered on antiviral/innate immune and unfolded-protein-response programs, with apoptosis and cholesterol homeostasis convergent only in discovery. Over-representation of the union of all layers recovered related core programs in both cohorts - p53, apoptosis, unfolded protein response, ribosome and cholesterol terms were significant in both - although the fraction of discovery-cohort terms also significant in validation ranged from 32% (WikiPathways) to 64% (Reactome) across the four databases. Notably, no pathway was significant only in the integration: the convergent programs were already strong in individual layers, and integration ranked them rather than revealing hidden ones - a restraint worth stating explicitly, since it delimits what integrative multi-layer analysis adds to this system.

The biological payoff of this convergence is a cell-death landscape broader than apoptosis alone. Beyond the splicing-centered, cross-cohort p53-apoptosis program of Sections 3–6, infection-associated remodeling extended to programmed-death programs of other mechanistic classes. Necroptosis-associated terms were enriched among splice-altered genes in the discovery cohort (KEGG necroptosis, FDR = 3.9×10^{-3}) and in the preranked GSEA of all expressed genes (NES +1.55, FDR = 0.035), yet the canonical executors *RIPK3* and *MLKL* were not detected in the GSC transcriptome of either cohort, restricting any necroptosis claim to pathway-level remodeling. Pyroptosis was supported at the executor-gene level: *CASP1* was strongly induced in discovery ($\log_2$FC +3.20, padj = 2×10^{-9}), *NLRP1* and *GSDMB* were padj-significant in the sub-threshold tier (NLRP1: padj = 8×10^{-7} in validation), with the GO pyroptosis term showing a suggestive threshold-free trend (NES +1.49, FDR = 0.124), while the Reactome defective-pyroptosis set was enriched in the repressed pole (NES -2.13, FDR = 3.3×10^{-4}); differential editing of *APAF1* and *CASP9* in the validation cohort added a regulatory layer over the same machinery (Section 5). Ferroptosis appeared exclusively in the splicing layer (KEGG FDR = 3.1×10^{-2}).

A final, previously unreported layer connects this death program to immune visibility: the host-ZIKV chimeric transcripts described above encode junction peptides present in neither parental proteome, and antigen processing and MHC class I assembly, the machinery that displays intracellular peptides at the cell surface for cytotoxic T-cell recognition, ranks second

among the pathways converged upon by at least two regulatory layers in this system (18.5% of its genes affected), raising, though not demonstrating, the possibility that the infected cell presents hybrid viral-human peptides at its surface. Taken together, the infected GSC state that emerges from the three layers is one of a vigorous interferon-driven antiviral transcriptional program, concomitant erosion of stem-cell identity markers, widespread directional splicing remodeling concentrated on RNA processing and p53-linked cell-death genes, and a stable background editome with induced ADAR but no reproducible differential editing, a multi-layer cellular state in which apoptosis is the best-supported death program, pyroptosis holds executor-level support, and necroptosis and ferroptosis remain pathway-level observations; which death modalities are ultimately executed is a question the transcriptional data alone cannot answer (Figure 7).

4. Discussion

Virological research demonstrates that Zika virus selectively kills GSCs (Zhu et al. 2017), driven in part by NS5, which suppresses glioma growth independently (Li et al. 2019) and directly interacts with or modulates host spliceosomal components (De Maio et al. 2016; Chen et al. 2023; Li et al. 2025). Conversely, tumor biology has established that GSCs are intrinsically addicted to RNA-processing machinery, displaying heightened vulnerability across lineage-specific alternative splicing (Ferrarese et al. 2014; Song et al. 2024), *ADAR1* dependence (Jiang et al. 2022), and synthetic lethality with spliceosome inhibitors (Fuentes-Fayos et al. 2022). Despite these converging lines of evidence, transcriptomic studies of infected brain tumors have read infection almost exclusively through differential gene expression, where interferon responses dominate by construction and cannot discriminate what the virus actively kills from what it merely alarms (Menezes et al. 2026; Singh et al. 2026). To bridge this conceptual divide, we formulate the hypothesis that ZIKV exploits the precise RNA-processing dependencies that define the stem cell state, and that post-transcriptional layers, rather than the antiviral transcriptome, carry the information most relevant to oncolysis, with NS5 acting as a candidate broker. Here, we integrate virological and tumor-biological evidence to evaluate this hypothesis and derive testable predictions.

A transcriptomic signature dominated by type I interferon and TNF is the expected output of innate sensing, and it appears wherever ZIKV replicates, across oncolytic transcriptomes of GBM lines (Singh et al. 2026), in systematic reviews of the field (Menezes et al. 2026), and in non-tumoral neural progenitors, where proviral and antiviral modules,

including *ADAR1* and *DDX3X*, coexist (Owaresat et al. 2026). Our data reproduce this echo in its purest form: per-sample interferon-alpha enrichment rose in every infected library of both cohorts. Yet the same literature supplies the reason this echo cannot discriminate what the virus kills from what it merely alarms, in neural progenitors, myeloid-derived interferon *restricts* infection rather than executing it (Bulstrode et al. 2022), protecting cells that ZIKV would otherwise kill. What is shared between killed and spared cells cannot explain selective killing; the antiviral transcriptome measures how loudly a cell announces infection, not why it dies. Two considerations sharpen this conclusion. First, the boundary between interferon signaling and the integrated stress response is genuinely blurred in flavivirus infection (Verma and Perlman 2025; Badu et al. 2026), so the attribution of individual genes to one program or the other is partly conventional. Second, and more decisive, the response is architecturally partitioned rather than uniform: genes induced at the expression level overlap splice-altered genes far less than chance (0.44-fold, $p = 3.3\text{x}10^{-30}$), whereas splicing and editing co-target genes more often than chance (1.75-fold, $p = 8.9\text{x}10^{-4}$). Infection, in other words, writes two largely disjoint programs, a transcriptional antiviral module and a cohesive post-transcriptional module, and only the second is a plausible carrier of the death decision.

GSCs are dependent on the splicing machinery as a matter of tumor biology: *SRSF3*-regulated alternative splicing promotes GBM progression (Song et al. 2019), splicing intersects *MYC* in synthetic lethality (Stine and Dang 2015), and pharmacological SF3B1 inhibition collapses GBM malignancy through *BCL2L1* splicing and mTOR/beta-catenin signaling, prolonging survival in preclinical models (Fuentes-Fayos et al. 2022). Viral manipulation of splicing had only one precedent, a ZIKV-infection study in neuroblastoma cells (Bonenfant et al. 2020), a mechanism with functional roots, since the viral subgenomic RNA alone sequesters splicing- and decay- regulatory RNA-binding proteins and compromises host splicing (Michalski et al. 2019), and sfRNA generation is required for productive infection of human cells (Pallarés et al. 2020); and our data extend it to GSCs with unusual robustness: the splicing layer reached roughly twice as many genes as the expression layer, and its most remodeled target in both cohorts was the core processing factor *HNRNPC*, the machinery rewriting itself, under conditions spanning two viral lineages (Dakar 41519 and PE243), two library layouts and different cell-line compositions. That splicing and editing co-target genes more often than chance (1.75-fold) indicates a coordinated post-transcriptional module rather than isolated events. We propose that viral remodeling of this machinery phenocopies its pharmacological collapse: the same synthetic-lethality principle that makes spliceosome inhibitors lethal to

GSCs would make viral saturation of the machinery lethal without any inhibitor. The window for this collapse is narrow, because *ATF4* both adapts GBM to hypoxia and temozolomide and feeds the pro-apoptotic arm of the integrated stress response (Lorenz et al. 2021), a shared axis that infection appears to tip from rescue toward death. This convergence nominates spliceosome inhibitors as rational combination partners for oncolytic ZIKV.

Zika virus-encoded proteins manipulate the p53 signaling axis through distinct structural and nonstructural mechanisms: the viral capsid interacts with MDM2 (Teng et al. 2017) and triggers RPL11-mediated ribosomal stress with p53 accumulation (Slomnicki et al. 2018), while NS5 binds the p53 C-terminal domain to interfere with MDM2-mediated degradation (Li et al. 2021). In our data, *TP53* mRNA was unchanged while its targets rose (*NOXA*/*PMAIP1* +3.75), whereas both negative regulators were remodeled at transcript architecture, *MDM2* across expression and a replicated exon-inclusion event (ΔPSI +0.46), and *MDM4* in splicing alone. This pairing with literature showing viral proteins engage this exact brake complex mirrors our observation that the brakes (not *TP53* itself) are what infection rewrites. In glioblastoma, p53 is frequently wild-type yet suppressed by noncanonical axes (EGFR–DNA-PKcs; (Ding et al. 2022)), making MDM2 an active drug target (Pellot Ortiz et al. 2023; Han et al. 2024); releasing p53 in GSCs is consequential, and our data suggest infection achieves this at the RNA level. However, *BAX* and *CYCS* declined, the validation-cohort reversal of one p53 gene set (-53, $p = 0.10$, minimum attainable) is inconclusive, and percent spliced-in is transcript-level, not protein. Furthermore, A-to-I editing of the *MDM2* 3′UTR regulates its expression (Almeric et al. 2025), bridging this axis to the editing layer. This convergence is consistent with post-transcriptional activation of the p53 brake system rather than with transcriptional induction of *TP53*.

Our transcriptomic analysis does not measure NS5 directly; rather, NS5 enters as the literature's answer to the question our data raise, why a flavivirus would systematically rewrite spliceosomal components and p53 negative regulators in a tumor intrinsically addicted to both. In GBM, ZIKV NS5 alone, without other viral components, reduces cell growth, sphere formation, and invasion while preventing orthotopic tumor formation, though its mechanism was left open (Li et al. 2019). Extending beyond the cytoplasm, NS5 forms nuclear bodies sequestering importin-α (Ng et al. 2019), requires nuclear accumulation for replication (Ji and Luo 2020), and binds chromatin to regulate host transcription (Li et al. 2022), whereas its canonical STAT2 degradation (Grant et al. 2016; Ren et al. 2024) explains why studies rarely looked beyond innate immunity. Regarding post-transcriptional crosstalk, Dengue virus

(DENV) NS5 intrudes into the spliceosome to modulate splicing (De Maio et al. 2016), whereas in ZIKV, NS5 binds the core spliceosomal factor SF3B3 (Chen et al. 2023), reduces SC35/SRSF2 protein (Li et al. 2025), and sequesters HSP90 (Hajari et al. 2025); thus, spliceosome intrusion is demonstrated for DENV and remains a prediction for ZIKV in GSCs. A second viral RNA entity compounds the brokerage: sfRNAs are not a by-product but a requirement for productive infection (Pallarés et al. 2020), and sfRNA alone compromises host splicing and mRNA decay through sequestration of RNA-binding proteins (Michalski et al. 2019), making the post-transcriptional rewrite a joint output of viral protein and viral RNA. Ultimately, NS5 is the most parsimonious candidate broker of this crosstalk, generating a testable hypothesis with two decisive predictions: NS5-deficient ZIKV should fail to remodel splicing in GSCs, whereas purified NS5 alone should phenocopy this post-transcriptional signature.

The chimeric transcripts add a molecular signature of this brokerage. The 813 host–viral junctions we recovered are not generated by the spliceosome their broker is accused of co-opting, breakpoint architecture excludes it (0.7% GT-AG, at chance frequency), but carry the four-to-ten-nucleotide microhomology of copy-choice RNA recombination (76%) (Lai 1992; Nagy and Simon 1997): the polymerase domain of NS5 itself, copying promiscuously at the replication complex, writes infection's own post-transcriptional layer one junction at a time, reproducibly across strains, lineages and cohorts. A precedent for functional host–viral chimeric products exists in influenza, where cap-snatched hybrids translate into chimeric proteins that generate T-cell responses and contribute to virulence (Ho et al. 2020); in SARS-CoV-2, chimeric transcripts were reported and contested as artifacts of reverse transcription (Zhang et al. 2021; Parry et al. 2021), our junctions differ from both, arising during RNA replication itself. Whether this layer carries functional weight in GSCs is open: junction-spanning open reading frames are present in most chimeras (713 of 813), without enrichment over simulated junctions, so junction peptides are structurally possible but not selected for; and antigen processing ranks second among our multi-layer convergent programs (18.5% of genes). We therefore raise immunogenicity as a hypothesis to be tested by HLA-bound peptidomics of infected GSCs, and add a third decisive prediction to the broker model, polymerase-deficient virus should abolish chimeric junction formation while leaving spliceosomal remodeling intact, dissociating the two candidate activities of NS5.

ADAR1 sits precisely where our hypothesis predicts: tumor biology shows it is essential to GSC maintenance (Jiang et al. 2022) within the broader cancer-editing landscape (Baysal et

al. 2017), while virology shows it is a proviral resource, ADAR1 promotes ZIKV replication by restraining PKR (Zhou et al. 2019), editing patterns shift in congenital ZIKV infection (Wales-McGrath et al. 2023), and ADAR-virus coevolution is long-standing (Samuel 2011; Piontkivska et al. 2021). Our data separates these two roles cleanly. The site-level response to infection did not replicate across cohorts ($p = 0.61$): where the splicing layer was rewritten at thousands of junctions, the editome proved a deeply buffered, stable layer, itself an informative asymmetry between two post-transcriptional processes. What infection reproducibly changed was *ADAR1* abundance itself, induced in both cohorts, the direction the proviral ADAR1-PKR axis predicts. The filtered candidate set nonetheless contains two leads: recoding candidates recurring at identical coordinates in both cohorts (*SH2B1* N>S, *CDK13* Q>R), called against dbSNP b151, the reference variant build of the REDItools/REDIportal pipelines, and held strictly as candidates pending orthogonal DNA confirmation, and validation-only differential sites in *APAF1* and *CASP9*. We therefore propose that ZIKV sequesters ADAR1 as a replication asset on a tumor-addicted cell, with the death-relevant cost carried by the splicing layer; the recoding candidates, if DNA-confirmed, would mark the points where the hijacked layer touches the death machinery. Perturbing ADAR1 in infected GSCs is the decisive test of this hijack model.

The executor of ZIKV-induced death is caspase-centered wherever it has been tested directly: the pan-caspase inhibitor Q-VD-OPh rescued nearly all virus-induced death in embryonal CNS tumors, demoting TNF and RIPK1 to secondary routes (Rosa-Ribeiro et al. 2025), and TRAIL-mediated apoptosis operates in neural progenitors (Lee et al. 2020). Against this executor the virus actively brakes: ZIKV suppresses *NLRP3* and *TNFAIP3* (A20) with NF-kB survival output (Li et al. 2025), the same study tying the brake to the splicing machinery by showing NS5 reduces SC35/SRSF2, Bcl-2 family proteins delay death (Turpin et al. 2019), flaviviruses dual-regulate apoptosis (Pan et al. 2021), Japanese encephalitis virus blocks PKR via NS2A (Tu et al. 2012), PKR activation limits oncolytic therapy through TGF-beta (Hong et al. 2023), and aggresome formation precedes death (Basu et al. 2026). Our data place the GSC squarely inside this tug-of-war: infection simultaneously elevated a death mediator (*CASP1*, +3.20) and a survival brake (*BIRC3*/cIAP2, +7.31), while the integrated-stress-response signature (*DDIT3* up, *ATF4* down) matched the UPR-hijacking literature. The inflammatory executor route couples to the chemokine summit of the response (CXCL8/CXCL3/CXCL10/CXCL11), and potentially to the chimeric layer: if junction peptides reach MHC class I, the pyroptotic GSC dies as a visible inflammatory target rather

than a silent one. Modalities must be ranked honestly: necroptosis remains pathway-level only (*RIPK3* and *MLKL* undetected), ferroptosis appears solely in the splicing layer, and pyroptosis holds padj-significant but sub-threshold executor support (*NLRP1*, most strongly in validation; *GSDMB*). We propose an exploitation-plus-collapse model in which viral brakes purchase replication time until post-transcriptional collapse, ISR-driven *DDIT3*/*NOXA* plus splicing disruption of the p53 brakes, exceeds brake capacity. The model predicts Q-VD-OPh rescue of infected GSCs and epistasis between splicing inhibition and caspase dependence, and nominates death timing, rather than its induction, as the therapeutic variable.

Susceptibility rooted in the neural progenitor state is a shared feature across neurotropic arboviruses rather than a unique property of ZIKV. For instance, Oropouche virus similarly infects human neural progenitor cells and alters brain organoid growth (Albert et al. 2026; Brum et al. 2026), demonstrating that stem-state targeting occurs among arboviruses without reported oncolysis. This stem-state tropism explains why GSCs are infected, governed by neural stem factors like *SOX2* and integrin αvβ5 (Zhu et al. 2020), yet selective killing requires specific viral determinants capable of exploiting the tumor's RNA-processing addiction within the temporal window governed by intracellular death brakes. Crucially, because both cohorts in our study comprise GSCs alone without non-tumoral neural progenitor or differentiated tumor controls, our transcriptomic datasets cannot independently establish selectivity, leaving that claim to rest on original functional reports (Zhu et al. 2017). From a clinical perspective, understanding how viral determinants intersect progenitor susceptibility highlights the imperative for progenitor-sparing strategies and supports the development of attenuated strains to optimize therapeutic safety (Victorio et al. 2024).

5. Conclusion

By integrating differential expression, alternative splicing, and A-to-I RNA editing across two independent cohorts spanning two viral lineages, this study redefines the mechanistic basis of Zika virus oncolysis in glioblastoma stem cells. The type I interferon program, though the dominant transcriptional output of infection in both cohorts, was indistinguishable in kind from the response elicited in non-tumoral neural cells and therefore cannot account for tumor-selective cytotoxicity. Selectivity emerged instead from the post-transcriptional layers. Alternative splicing was remodeled at thousands of reproducible junctions, preferentially targeting the RNA-processing machinery on which glioblastoma stem cells are uniquely dependent, and converging on the p53 regulatory axis at its most vulnerable

point: the transcript architecture of its principal inhibitors, MDM2 and MDM4, with a replicated exon-inclusion event falling wholly within the p53-binding domain. RNA editing, by contrast, proved a buffered and stable layer, reproducibly altered only in the induction of ADAR1 itself, consistent with viral co-option of an editing enzyme as a replication asset rather than broad reprogramming of the editome. A newly detected class of host–viral chimeric transcripts, generated by template switching of the viral RNA-dependent RNA polymerase and replicated across cohorts and strains, extends this post-transcriptional reprogramming to transcripts that exist in neither genome alone. Together, these observations support a model in which ZIKV exploits the RNA-processing dependency of the GSC state, pharmacologically validated as synthetic-lethal by spliceosome inhibitors, through a convergence of spliceosomal disruption, p53 brake remodeling, translational shutdown of short-lived survival proteins, and pyroptotic executor induction. Therefore, rather than acting exclusively through direct viral cytotoxicity or a conventional apoptotic pathway, ZIKV may selectively exploit the molecular and functional dependencies of GSCs by simultaneously disrupting translational homeostasis, post-transcriptional regulation, survival signaling, and stemness-associated programs. The resulting convergence of p53-associated cell-death signaling, potential inflammatory execution mechanisms, and loss of tumor stem-cell identity provides an integrated explanation for ZIKV-induced oncolysis and establishes a mechanistic framework for investigating the molecular basis of its selectivity toward glioblastoma stem-like populations.

Figure 1. Sequencing quality, infection-specific alignment reduction, and global transcriptional response to ZIKV infection in glioblastoma stem cells. (A) Per-library alignment rates against the transcript-aware GRCh38 index, shown as paired dumbbells connecting each mock library (blue) to its matched ZIKV-infected library (red) in the discovery cohort (six line-matched pairs, percentage of reads) and the validation cohort (three pairs, percentage of read pairs). Alignment was uniformly high in mock libraries (discovery 96.6–98.6%; validation 80.9–82.3%) and selectively reduced in infected libraries (discovery 65.5–79.6%, a reduction of 17–32 percentage points against line-matched controls; validation 45.5–54.1%, 27–36 points against the mock mean); in both cohorts the reduction was confined to infected libraries and tracked infection status rather than sequencing depth. **(B)** Volcano plot of differential expression (ZIKV versus mock) in the discovery cohort (DESeq2; all 17,478 tested genes), $\log_2$ fold-change *versus* -log10 adjusted P (padj). Gray, non-significant; red, induced (padj < 0.05, $\log_2$FC >= 1.5); blue, repressed (padj < 0.05, $\log_2$FC <= 1.5); dashed lines mark the significance and effect-size thresholds (padj = 0.05; $|\log_2 FC| = 1.5$). Of 1,512

differentially expressed genes, 1,216 were induced and 296 repressed. **(C)** Heat map of the 50 most induced genes (ranked by log2 fold-change; rows, gene symbols) across all 12 discovery libraries (columns; six mock, six ZIKV-infected, three GSC lines), on variance-stabilized (VST) z-scored expression (red, above line mean; blue, below).

Figure 2. Pathway-level architecture of the ZIKV-infected GSC transcriptome: over-representation and threshold-free enrichment, discovery and validation cohorts. (A) Over-representation analysis (ORA) of the 1,216 induced genes (hypergeometric test against the background of all expressed genes; FDR < 0.05) across four curated databases, shown as the top-ranked terms per database (horizontal bars, -log10 FDR; bar color encodes database: GO Biological Process, KEGG, Reactome, WikiPathways). The number of induced genes in each term relative to term size (k/n) is annotated at each bar end. The landscape is dominated by antiviral and inflammatory programs of 873 significant terms in total (GO 454, KEGG 119, Reactome 117, WikiPathways 183). **(B)** Pre-ranked gene set enrichment analysis (GSEA) of the discovery cohort, ranking all 17,478 expressed genes by the DESeq2 Wald statistic (sign × significance; threshold-free), shown as diverging horizontal bars of Normalized Enrichment Score (NES) for the leading induced (positive) and repressed (negative) pathways (all FDR < 0.001; x = 0 reference line). The induced pole is led by convergent antiviral signals across databases, whereas translation dominates the repressed pole, indicating a genome-wide shutdown of the translational machinery accompanying the antiviral program. **(C)** Validation-cohort pre-ranked GSEA (same Wald-statistic ranking and encoding as in B). Both poles reproduce: the antiviral-inflammatory extreme and a deepened translational shutdown, extending the repressed pole from translation to ribosome biogenesis and splicing machinery (all FDR < 0.001).

Figure 3. ZIKV infection induces profound and reproducible alternative splicing remodeling in GSCs. (A) Significant splicing events (junction counts and exon body coverage; FDR < 0.05) across the five event classes, skipped exon (SE), retained intron (RI), alternative 5′ splice site (A5SS), alternative 3′ splice site (A3SS), mutually exclusive exon (MXE), shown as event counts per class, with bars partitioned by directional effect in the infected state (higher inclusion versus higher skipping/switching). Of 6,749 significant events across 3,036 genes, twice as many genes as the differential expression layer, SE was the largest class (3,028), followed by RI (1,178), A5SS (962), MXE (828) and A3SS (753); the direction was skewed toward loss of canonical annotation: skipping exceeded inclusion among SE events (1,741 vs 1,286), 72% of A5SS events shifted away from the annotated 5′ site, and retained introns were

more often lost than gained (691 vs 487), a pattern consistent with reduced spliceosome fidelity upon infection. **(B)** Genes carrying the heaviest splicing burden in the discovery dataset in red (top 15 by number of significant events; horizontal bars, event counts; gene symbols), annotated with the count of significant events for the same gene in the validation cohort (blue). Six of the ten most event-dense discovery genes reappear among the most affected in validation (*HNRNPC* remains the top gene genome-wide (71 events), followed by shared *WARS1*, *SNHG17*, *PFDN5*, *GAS5* and *EEF1D*, joined by *AKAP8L*, ranked 15th in discovery but top-tier in validation; 1,356 genes (44.7% of the discovery set) are splice-altered in both cohorts (hypergeometric $p \approx 0$). The list is dominated by components of the RNA-processing machinery itself and genes coupling transcription to translation, indicating that infection remodels the regulators of the very process being disrupted. **(C)** Over-representation analysis of the 3,036 splice-altered genes (hypergeometric test; FDR < 0.05; horizontal bars, -log10 FDR, bar color per database; k/n annotated at bar ends), summarized as the top three terms per database plus three prespecified p53/cell-death terms (hatched) Within this landscape, the prespecified cell-death terms are prominently enriched, transcriptional regulation by TP53, programmed cell death and apoptosis, establishing p53-linked cell-death genes as a preferential target of infection-associated splicing remodeling.

Figure 4. Event-level replication of splicing remodeling across cohorts: coordinate-paired concordance, effect-size correlation, and attenuation. (A) Cross-cohort concordance of the 1,063 splicing events significant in both cohorts (rMATS FDR < 0.05 each), paired by full coordinate signature (event type, chromosome, strand and all splice junction coordinates) since rMATS event identifiers are run-specific. ΔPSI in the discovery cohort (x-axis) versus ΔPSI in the validation cohort (y-axis); positive ΔPSI = higher inclusion in infected libraries. Color encodes directional concordance; the identity line is shown for reference. Direction was concordant in 95.9% of events (1,019/1,063) and effect sizes correlated strongly between cohort. **(B)** Directional concordance by event class, for the same replicated events (horizontal bars, % concordant; dashed line, 50% chance expectation; n per class annotated). Concordance is uniformly high across classes and replicated events map to 617 distinct genes. When an event is significant in both cohorts, its direction is essentially determined, establishing a layer of splicing regulation that survives changes in cell-line composition (three lines *versus* one), library layout (single- versus paired-end), depth and infection protocol. **(C)** Effect-size attenuation between cohorts. |ΔPSI| in the validation cohort versus |ΔPSI| in the discovery cohort for the replicated events (gray points), with the binned median (red line) against the

identity expectation (dashed); the median attenuation slope is annotated. The MDM2 anchor event (chr12:68816811-68816945, exon lying wholly within the N-terminal p53-binding domain, amino acids 53–96) is highlighted: increased inclusion upon infection in both cohorts, with the attenuated validation magnitude consistent with the reduced statistical power of three replicates per group. Beyond anchor cases, most concordant genes are hit by different specific events in each cohort, gene-level convergence without event-level identity, indicating that infection directs its splicing program at the level of target genes rather than individual splice junctions, with a core of ~1,000 junction-level changes robust enough to recur under independent experimental conditions.

Figure 5. The A-to-I editome in ZIKV-infected GSCs: a conserved background, region-biased differential sites, and absence of reproducible differential editing. (A) Conservation of the background editome across cohorts. Editing frequency (A-to-G) at sites shared between the discovery and validation calling runs, discovery versus validation (scatter; identity line for reference; Pearson r annotated). Despite an eight-fold difference in detection depth (838 reproducible sites in discovery; 7,162 in paired-end validation), 68.5% of discovery aggregated sites were recovered in validation with near-identical frequencies ($r = 0.989 – 0.993$ in the cross-implementation benchmark), the background editome is a conserved, stable layer of the infected-cell transcriptome. **(B)** Genomic distribution of differentially edited sites (138 discovery; 1,665 validation), partitioned by region (stacked 100% bars per cohort; percentage labels; n annotated). Differential sites are predominantly located in regulatory regions and the validation cohort placed four sites in cell-death executor genes (three in APAF1, one in CASP9, the latter within coding sequence). **(C)** Differential editing does not replicate beyond chance. Overlap of differentially edited sites between cohorts (observed versus hypergeometric expectation; p annotated): 21.7% of the discovery set overlapped ($p = 0.61$), and although 73.2% of discovery differential sites remained edited at the aggregated level in validation, direction agreed in only 24 of 30 evaluable replicated sites.

Figure 6. Per-sample activity of six prespecified transcriptional programs places p53 activation within a coordinated multi-program response to ZIKV infection. Per-sample ssGSEA enrichment scores for six prespecified axes, p53 pathway (MSigDB Hallmark), interferon-alpha response, TNF/NF-κB signaling, E2F/cell-cycle, ribosome/translation, and the GSC/stemness marker set, in the discovery cohort (six panels; boxplots, median and interquartile range, whiskers 1.5×IQR, individual libraries as points; infected versus mock). The p53 axis is quantified at every level in the text: per-sample Hallmark enrichment increased

in every infected library relative to every control (mean difference +765 enrichment units; exact Wilcoxon p = 0.0022, the value attained by perfect 6-*versus*-6 separation). Infection concurrently activated TNF/NF-κB, repressed E2F/cell-cycle and ribosome/translation programs, and lowered the stemness score (all BH $q < 0.05$): p53 activation occurred within a coordinated multi-program state rather than in isolation, alongside concomitant (not sequential) erosion of stem-cell markers. P values are from exact two-sided unpaired Wilcoxon tests; q values Benjamini-Hochberg-adjusted across the six axes; Δ = mean(ZIKV) - mean(Control) per axis.

Figure 7. Integrated post-transcriptional mechanistic model of Zika virus (ZIKV)-induced selective oncolysis in glioblastoma stem cells (GSCs). (A) Generic Antiviral Alarm (Transcriptional Layer). Viral entry and cytosolic sensing by MDA5 (*IFIH1*) trigger a robust type I and III interferon (*IFNB1*) transcriptional cascade and downstream ISG induction (*OASL*, *IFIT1*, *MX2*), alongside TNF/NF-κB inflammatory signaling. However, cytosolic NS5 targets STAT2 for proteasomal degradation, crippling heterotrimeric ISGF3 (STAT1–STAT2–IRF9) assembly required to establish an effective protective antiviral state. Consequently, the strong transcriptional IFN induction acts merely as a generic, non-discriminatory "cellular alarm" that is neutralized at the protein level, failing on its own to account for tumor-selective cytotoxicity and shifting the execution fate to nuclear post-transcriptional events. **(B) Post-Transcriptional Remodeling and Proviral Sequestration (Discriminant Layer).** Extending beyond the cytoplasm, NS5 forms nuclear bodies sequestering importin-α, requires nuclear accumulation for viral replication, and binds chromatin to regulate host transcription. Within the nucleus of GSCs, NS5 targets core spliceosomal factors (SF3B3, SRSF2), driving widespread alternative splicing disruption (>6,700 events across >3,000 genes, including HNRNPC). This perturbation exploits the addiction of GSCs to precise alternative splicing for stemness maintenance, inducing synthetic lethality. Simultaneously, the critical negative regulators of p53, MDM2 and MDM4, undergo structural transcript remodeling, while ADAR1 is co-opted to buffer the A-to-I editome and restrain PKR activation, shifting the functional death burden to the splicing layer. **(C) Post-Transcriptional p53 Release, Intracellular Tug-of-War, and Caspase Execution.** Remodeling of the MDM2/MDM4 brake architecture, coupled with direct physical binding between the MTase domain of NS5 and the C-terminal domain of p53, stabilizes p53 protein and liberates its transactivation potential post-transcriptionally without altering TP53 mRNA levels. This dual post-transcriptional mechanism drives key pro-apoptotic downstream

effectors (PMAIP1/NOXA, DDIT3/CHOP). Infected GSCs navigate a dynamic intracellular tug-of-war between viral survival checkpoints (BIRC3, TNFAIP3/A20) and accumulating proteotoxic/splicing stress. Once post-transcriptional collapse exceeds brake capacity, cell death is executed via a pan-caspase-dependent pathway (rescuable by Q-VD-OPh).

Supplementary Information: The online version contains supplementary material available.

Author contributions: I.N.S., C.V.M.S., and G.N. performed the bioinformatics and statistical analyses of the discovery dataset, interpreted the results, and contributed to manuscript writing. L.C.M. and A.S.P.L. performed the bioinformatics and statistical analyses of the validation dataset, interpreted the results, and contributed to manuscript writing. A.G. conceptualized and designed the study, oversaw its overall scientific integrity, and critically revised the manuscript. All authors read and approved the final version of the manuscript.

Funding: This study was financed in part by the Coordenação de Aperfeiçoamento de Pessoal de Nível Superior - Brasil (CAPES) - Finance Code 001

Conflicts of Interest: The authors declare no competing interests.

6. References

Albert A, Couture L, Piumi F, et al (2026) Oropouche virus infects human neural progenitor cells and alters the growth of brain organoids. iScience 29:114957. https://doi.org/10.1016/j.isci.2026.114957

Almeric E, Karagozoglu D, Cicek M, et al (2025) 3'UTR RNA editing driven by ADAR1 modulates MDM2 expression in breast cancer cells. Funct Integr Genomics 25:103. https://doi.org/10.1007/s10142-025-01611-3

Alves AL V., Gomes INF, Carloni AC, et al (2021) Role of glioblastoma stem cells in cancer therapeutic resistance: a perspective on antineoplastic agents from natural sources and chemical derivatives. Stem Cell Res Ther 12:206. https://doi.org/10.1186/s13287-021-02231-x

Badu P, González ETC, Pager CT (2026) Cellular Responses to Flavivirus Infections: Stress Signaling at the Crossroads of Host Defense and Virus Infection. Viruses 18:748. https://doi.org/10.3390/v18070748

Basu M, Espínola EE, Niu W, et al (2026) West Nile virus and Zika virus infections induce aggresome formation in human neural progenitor and A549 cells. J Virol 100:. https://doi.org/10.1128/jvi.02080-25

Baysal BE, Sharma S, Hashemikhabir S, Janga SC (2017) RNA Editing in Pathogenesis of Cancer. Cancer Res 77:3733–3739. https://doi.org/10.1158/0008-5472.CAN-17-0520

Ben Mrid R, El Guendouzi S, Mineo M, El Fatimy R (2025) The emerging roles of aberrant alternative splicing in glioma. Cell Death Discov 11:50. https://doi.org/10.1038/s41420-025-02323-0

Best SM (2017) The Many Faces of the Flavivirus NS5 Protein in Antagonism of Type I Interferon Signaling. J Virol 91:. https://doi.org/10.1128/JVI.01970-16

Bonenfant G, Meng R, Shotwell C, et al (2020) Asian Zika Virus Isolate Significantly Changes the Transcriptional Profile and Alternative RNA Splicing Events in a Neuroblastoma Cell Line. Viruses 12:. https://doi.org/10.3390/v12050510

Brum G, Grizente V, Lima Monteiro FL, et al (2026) Microcephaly-like phenotype triggered by novel reassortant and prototypic Oropouche virus strains in brain organoids. EBioMedicine 130:106408. https://doi.org/10.1016/j.ebiom.2026.106408

Bulstrode H, Girdler GC, Gracia T, et al (2022) Myeloid cell interferon secretion restricts Zika flavivirus infection of developing and malignant human neural progenitor cells. Neuron 110:3936-3951.e10. https://doi.org/10.1016/j.neuron.2022.09.002

Chen T, Yang H, Liu P, et al (2023) Splicing factor SF3B3, a NS5-binding protein, restricts ZIKV infection by targeting GCH1. Virol Sin 38:222–232. https://doi.org/10.1016/j.virs.2022.12.005

De Maio FA, Risso G, Iglesias NG, et al (2016) The Dengue Virus NS5 Protein Intrudes in the Cellular Spliceosome and Modulates Splicing. PLoS Pathog 12:e1005841. https://doi.org/10.1371/journal.ppat.1005841

Ding J, Li X, Khan S, et al (2022) EGFR suppresses p53 function by promoting p53 binding to DNA-PKcs: a noncanonical regulatory axis between EGFR and wild-type p53 in glioblastoma. Neuro Oncol 24:1712–1725. https://doi.org/10.1093/neuonc/noac105

Dome A, Dymova M, Richter V, Stepanov G (2022) Post-Transcriptional Modifications of RNA as Regulators of Apoptosis in Glioblastoma. Int J Mol Sci 23:9272. https://doi.org/10.3390/ijms23169272

Ferrarese R, Harsh GR, Yadav AK, et al (2014) Lineage-specific splicing of a brain-enriched alternative exon promotes glioblastoma progression. Journal of Clinical Investigation 124:2861–2876. https://doi.org/10.1172/JCI68836

Francipane MG, Douradinha B, Chinnici CM, et al (2021) Zika Virus: A New Therapeutic Candidate for Glioblastoma Treatment. Int J Mol Sci 22:10996. https://doi.org/10.3390/ijms222010996

Fuentes-Fayos AC, Pérez-Gómez JM, G-García ME, et al (2022) SF3B1 inhibition disrupts malignancy and prolongs survival in glioblastoma patients through BCL2L1 splicing and mTOR/ß-catenin pathways imbalances. Journal of Experimental & Clinical Cancer Research 41:39. https://doi.org/10.1186/s13046-022-02241-4

Garcia G, Chakravarty N, Paiola S, et al (2023) Differential Susceptibility of Ex Vivo Primary Glioblastoma Tumors to Oncolytic Effect of Modified Zika Virus. Cells 12:2384. https://doi.org/10.3390/cells12192384

Grant A, Ponia SS, Tripathi S, et al (2016) Zika Virus Targets Human STAT2 to Inhibit Type I Interferon Signaling. Cell Host Microbe 19:882–90. https://doi.org/10.1016/j.chom.2016.05.009

Hajari N, Knoll M, Lu A, et al (2025) The Zika virus NS5 protein binds HSP90 to suppress EGF-induced Akt signaling and trophoblast cell migration. Virology 603:110370. https://doi.org/10.1016/j.virol.2024.110370

Han M, Kakar M, Li W, et al (2024) Targeting MDM2-p53 interaction in Glioblastoma: Transcriptomic analysis and Peptide-Based inhibition strategy. Bioorg Chem 150:107620. https://doi.org/10.1016/j.bioorg.2024.107620

Ho JSY, Angel M, Ma Y, et al (2020) Hybrid Gene Origination Creates Human-Virus Chimeric Proteins during Infection. Cell 181:1502-1517.e23. https://doi.org/10.1016/j.cell.2020.05.035

Hong B, Sahu U, Mullarkey MP, et al (2023) PKR induces TGF-β and limits oncolytic immune therapy. J Immunother Cancer 11:e006164. https://doi.org/10.1136/jitc-2022-006164

Iannolo G, Sciuto MR, Cuscino N, et al (2019) Zika virus infection induces MiR34c expression in glioblastoma stem cells: new perspectives for brain tumor treatments. Cell Death Dis 10:263. https://doi.org/10.1038/s41419-019-1499-z

Ji W, Luo G (2020) Zika virus NS5 nuclear accumulation is protective of protein degradation and is required for viral RNA replication. Virology 541:124–135. https://doi.org/10.1016/j.virol.2019.10.010

Jiang L, Hao Y, Shao C, et al (2022) ADAR1-mediated RNA editing links ganglioside catabolism to glioblastoma stem cell maintenance. J Clin Invest 132:. https://doi.org/10.1172/JCI143397

Lai MM (1992) RNA recombination in animal and plant viruses. Microbiol Rev 56:61–79. https://doi.org/10.1128/mr.56.1.61-79.1992

Lee JK, Kim J-A, Oh S-J, et al (2020) Zika Virus Induces Tumor Necrosis Factor-Related Apoptosis Inducing Ligand (TRAIL)-Mediated Apoptosis in Human Neural Progenitor Cells. Cells 9:2487. https://doi.org/10.3390/cells9112487

Li C, Xu D, Ye Q, et al (2016) Zika Virus Disrupts Neural Progenitor Development and Leads to Microcephaly in Mice. Cell Stem Cell 19:120–126. https://doi.org/10.1016/j.stem.2016.04.017

Li H, Hu Y, Huang J, et al (2019) Zika virus NS5 protein inhibits cell growth and invasion of glioma. Biochem Biophys Res Commun 516:515–520. https://doi.org/10.1016/j.bbrc.2019.06.064

Li J, Zhu C, Meng Y, et al (2025) Zika virus inhibits cell death by inhibiting the expression of NLRP3 and A20. J Virol 99:. https://doi.org/10.1128/jvi.01980-24

Li P, Jiang H, Peng H, et al (2021) Non-Structural Protein 5 of Zika Virus Interacts with p53 in Human Neural Progenitor Cells and Induces p53-Mediated Apoptosis. Virol Sin 36:1411–1420. https://doi.org/10.1007/s12250-021-00422-7

Li P, Wu J, Liu S, et al (2022) The RNA polymerase of cytoplasmically replicating Zika virus binds with chromatin DNA in nuclei and regulates host gene transcription. Proceedings of the National Academy of Sciences 119:. https://doi.org/10.1073/pnas.2205013119

Lorenz NI, Sittig ACM, Urban H, et al (2021) Activating transcription factor 4 mediates adaptation of human glioblastoma cells to hypoxia and temozolomide. Sci Rep 11:14161. https://doi.org/10.1038/s41598-021-93663-1

Menezes D, Reis CR, Mamede I, et al (2026) Transcriptomic Profile of Glioblastoma Cells Infected with Zika Virus: A Systematic Review and Pathway Analysis. Viruses 18:249. https://doi.org/10.3390/v18020249

Michalski D, Ontiveros JG, Russo J, et al (2019) Zika virus noncoding sfRNAs sequester multiple host-derived RNA-binding proteins and modulate mRNA decay and splicing during infection. Journal of Biological Chemistry 294:16282–16296. https://doi.org/10.1074/jbc.RA119.009129

Nagy PD, Simon AE (1997) New Insights into the Mechanisms of RNA Recombination. Virology 235:1–9. https://doi.org/10.1006/viro.1997.8681

Ng IHW, Chan KW-K, Tan MJA, et al (2019) Zika Virus NS5 Forms Supramolecular Nuclear Bodies That Sequester Importin-α and Modulate the Host Immune and Pro-Inflammatory Response in Neuronal Cells. ACS Infect Dis 5:932–948. https://doi.org/10.1021/acsinfecdis.8b00373

Owaresat JK, Dey D, Siam MdAH, et al (2026) Comparative Gene Co-expression Network Analysis of Proviral and Antiviral Responses to Dengue Virus-2 (DENV-2) and Zika Virus (ZIKV) Infection in Human Neural Progenitor Cells (hNPCs). PLoS One 21:e0347540. https://doi.org/10.1371/journal.pone.0347540

Pallarés HM, Costa Navarro GS, Villordo SM, et al (2020) Zika Virus Subgenomic Flavivirus RNA Generation Requires Cooperativity between Duplicated RNA Structures That Are Essential for Productive Infection in Human Cells. J Virol 94:. https://doi.org/10.1128/JVI.00343-20

Pan Y, Cheng A, Wang M, et al (2021) The Dual Regulation of Apoptosis by Flavivirus. Front Microbiol 12:. https://doi.org/10.3389/fmicb.2021.654494

Parry R, Gifford RJ, Lytras S, et al (2021) No evidence of SARS-CoV-2 reverse transcription and integration as the origin of chimeric transcripts in patient tissues. Proceedings of the National Academy of Sciences 118:. https://doi.org/10.1073/pnas.2109066118

Pellot Ortiz KI, Rechberger JS, Nonnenbroich LF, et al (2023) MDM2 Inhibition in the Treatment of Glioblastoma: From Concept to Clinical Investigation. Biomedicines 11:1879. https://doi.org/10.3390/biomedicines11071879

Piontkivska H, Wales-McGrath B, Miyamoto M, Wayne ML (2021) ADAR Editing in Viruses: An Evolutionary Force to Reckon with. Genome Biol Evol 13:. https://doi.org/10.1093/gbe/evab240

Piperi C, Markouli M, Gargalionis AN, et al (2023) Deciphering glioma epitranscriptome: focus on RNA modifications. Oncogene 42:2197–2206. https://doi.org/10.1038/s41388-023-02746-y

Ren W, Fu C, Zhang Y, et al (2024) Zika virus NS5 protein inhibits type I interferon signaling via CRL3 E3 ubiquitin ligase-mediated degradation of STAT2. Proceedings of the National Academy of Sciences 121:. https://doi.org/10.1073/pnas.2403235121

Rosa-Ribeiro R, Falco ML, Sena de Souza J, et al (2025) Unraveling Zika virus-induced cell death pathways in eradicating embryonal central nervous system tumors. Neuroscience 582:126–133. https://doi.org/10.1016/j.neuroscience.2025.07.039

Samuel CE (2011) ADARs: Viruses and Innate Immunity. pp 163–195

Sanami S, Banihashemian SZ, Amirpour S, et al (2025) Neuroteratogenic mechanisms of Zika virus (ZIKV) infection: Insights into fetal brain development disruption and congenital Zika syndrome: A systematic review. Mol Aspects Med 106:101418. https://doi.org/10.1016/j.mam.2025.101418

Sarrazin E, Valable S, Pérès EA, et al (2026) Glioblastoma and resistance to radiotherapy: role of cancer stem cells subpopulations, hypoxia and therapeutic strategies. Cancer Treat Rev 149:103198. https://doi.org/10.1016/j.ctrv.2026.103198

Singh S, Gerlein M, Horvath AR, et al (2026) Transcriptomic Meta-Analysis and Functional Validation Identify Long Non-Coding RNAs as Modulators of Zika Virus-Mediated Oncolysis in Glioblastoma Multiforme Cell Lines. Cells 15:1088. https://doi.org/10.3390/cells15121088

Slomnicki LP, Hallgren J, Vashishta A, et al (2018) Proapoptotic Requirement of Ribosomal Protein L11 in Ribosomal Stress-Challenged Cortical Neurons. Mol Neurobiol 55:538–553. https://doi.org/10.1007/s12035-016-0336-y

Song X, Tiek D, Miki S, et al (2024) RNA splicing analysis deciphers developmental hierarchies and reveals therapeutic targets in adult glioma. Journal of Clinical Investigation 134:. https://doi.org/10.1172/JCI173789

Song X, Wan X, Huang T, et al (2019) SRSF3-Regulated RNA Alternative Splicing Promotes Glioblastoma Tumorigenicity by Affecting Multiple Cellular Processes. Cancer Res 79:5288–5301. https://doi.org/10.1158/0008-5472.CAN-19-1504

Stine ZE, Dang CV (2015) Splicing and Dicing MYC-Mediated Synthetic Lethality. Cancer Cell 28:405–406. https://doi.org/10.1016/j.ccell.2015.09.016

Teng Y, Liu S, Guo X, et al (2017) An Integrative Analysis Reveals a Central Role of P53 Activation via MDM2 in Zika Virus Infection Induced Cell Death. Front Cell Infect Microbiol 7:. https://doi.org/10.3389/fcimb.2017.00327

Tu Y-C, Yu C-Y, Liang J-J, et al (2012) Blocking Double-Stranded RNA-Activated Protein Kinase PKR by Japanese Encephalitis Virus Nonstructural Protein 2A. J Virol 86:10347–10358. https://doi.org/10.1128/JVI.00525-12

Turpin J, Frumence E, Desprès P, et al (2019) The ZIKA Virus Delays Cell Death Through the Anti-Apoptotic Bcl-2 Family Proteins. Cells 8:1338. https://doi.org/10.3390/cells8111338

Verma AK, Perlman S (2025) Unraveling the complexities of neurotropic virus infection and immune evasion. Microbiology and Molecular Biology Reviews 89:. https://doi.org/10.1128/mmbr.00185-23

Victorio CBL, Novera W, Ganasarajah A, et al (2024) Repurposing of Zika virus live-attenuated vaccine (ZIKV-LAV) strains as oncolytic viruses targeting human glioblastoma multiforme cells. J Transl Med 22:. https://doi.org/10.1186/s12967-024-04930-4

Wales-McGrath B, Mercer H, Piontkivska H (2023) Changes in ADAR RNA editing patterns in CMV and ZIKV congenital infections. BMC Genomics 24:685. https://doi.org/10.1186/s12864-023-09778-4

Wang B, Thurmond S, Hai R, Song J (2018) Structure and function of Zika virus NS5 protein: perspectives for drug design. Cellular and Molecular Life Sciences 75:1723–1736. https://doi.org/10.1007/s00018-018-2751-x

Yoshida GJ, Saya H (2016) Therapeutic strategies targeting cancer stem cells. Cancer Sci 107:5–11. https://doi.org/10.1111/cas.12817

Zhang L, Richards A, Barrasa MI, et al (2021) Reverse-transcribed SARS-CoV-2 RNA can integrate into the genome of cultured human cells and can be expressed in patient-derived tissues. Proceedings of the National Academy of Sciences 118:. https://doi.org/10.1073/pnas.2105968118

Zhao Z, Tao M, Han W, et al (2021) Nuclear localization of Zika virus NS5 contributes to suppression of type I interferon production and response. Journal of General Virology 102:. https://doi.org/10.1099/jgv.0.001376

Zhou S, Yang C, Zhao F, et al (2019) Double-stranded RNA deaminase ADAR1 promotes the Zika virus replication by inhibiting the activation of protein kinase PKR. Journal of Biological Chemistry 294:18168–18180. https://doi.org/10.1074/jbc.RA119.009113

Zhu Z, Gorman MJ, McKenzie LD, et al (2017) Zika virus has oncolytic activity against glioblastoma stem cells. Journal of Experimental Medicine 214:2843–2857. https://doi.org/10.1084/jem.20171093

Zhu Z, Mesci P, Bernatchez JA, et al (2020) Zika Virus Targets Glioblastoma Stem Cells through a SOX2-Integrin αvβ5 Axis. Cell Stem Cell 26:187-204.e10. https://doi.org/10.1016/j.stem.2019.11.016

A

DISCOVERY (n=6 mock / n=6 ZIKV)

paired drop 17–32 pp

Pair 1 97.7 77.1

Pair 2 97.3 79.2

Pair 3 96.6 79.6

Pair 4 97.6 78.9

Pair 5 97.6 65.5

Pair 6 98.6 70.3

VALIDATION (n=3 mock / n=3 ZIKV)

paired drop 27–36 pp

Pair 1 80.9 45.5

Pair 2 81.7 54.1

Pair 3 82.3 54.1

Mock

ZIKV

100 80 60 40 20 0

Alignment rate (%)

B

-log10 adjusted p-value

300 250 200 150 100 50 0

-4 -2 -0 2 4 6 8 10

log 2 fold change (ZIKV / Control)

Upregulated (n = 1,216)

Downregulated (n = 296)

Not significant

C

Condition

Cell line

MX2 GCA GBP5 RSAD2 OAS2 CLEC17A lncRNA_244953 IFNL3 NEURL3 ANO9 CXCL8 IFNL2 ITGAM VIPR2 SERPINA6 UBASH3A LINC00944 GBP4 lncRNA_295226 CCL20 NOD2 CCL5-AS1 lncRNA_294658 RTP4 TNF lncRNA_305358 IFIT2 IFIH1 DHX58 CCL5 OASL HOXD10 CXCL10 IFIT1 VCAM1 IFNL1 BCO1 TAC3 SELE IFNB1 BIRC3 ICAM1 HTR3E C3 CXCL11 RAET1L TNFRSF9 CXCL3 IL32 IFI44

S16.G4121 S13.G0387 S09.G3565 S08.G3565 S12.G0387 S17.G4121 S14.G0387 S15.G0387 S10.G3565 S11.G3565 S18.G4121 S19.G4121

Control

ZIKV

GSC3565

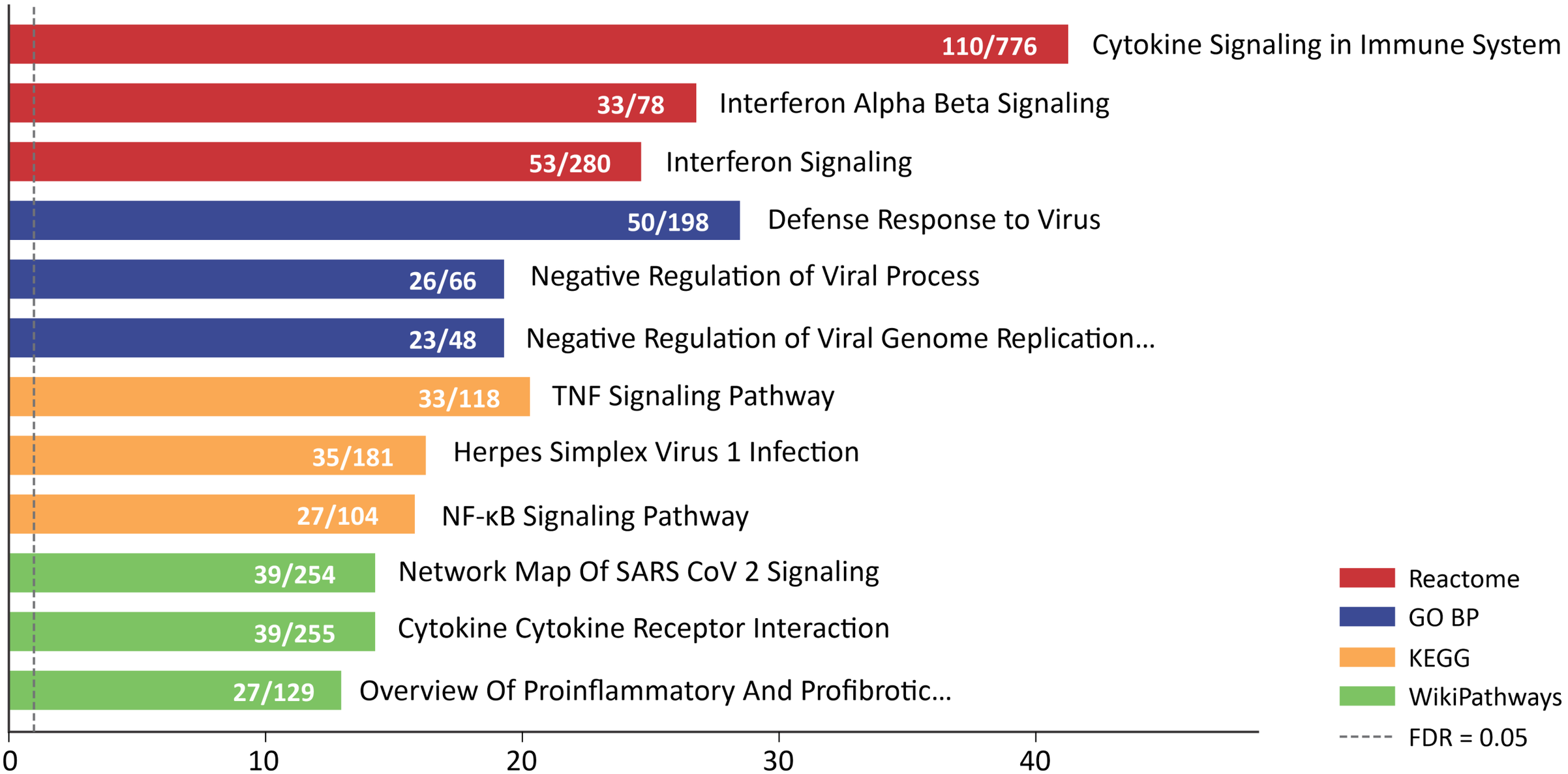
GSC0387

GSC4121

−2 −1 0 1 2

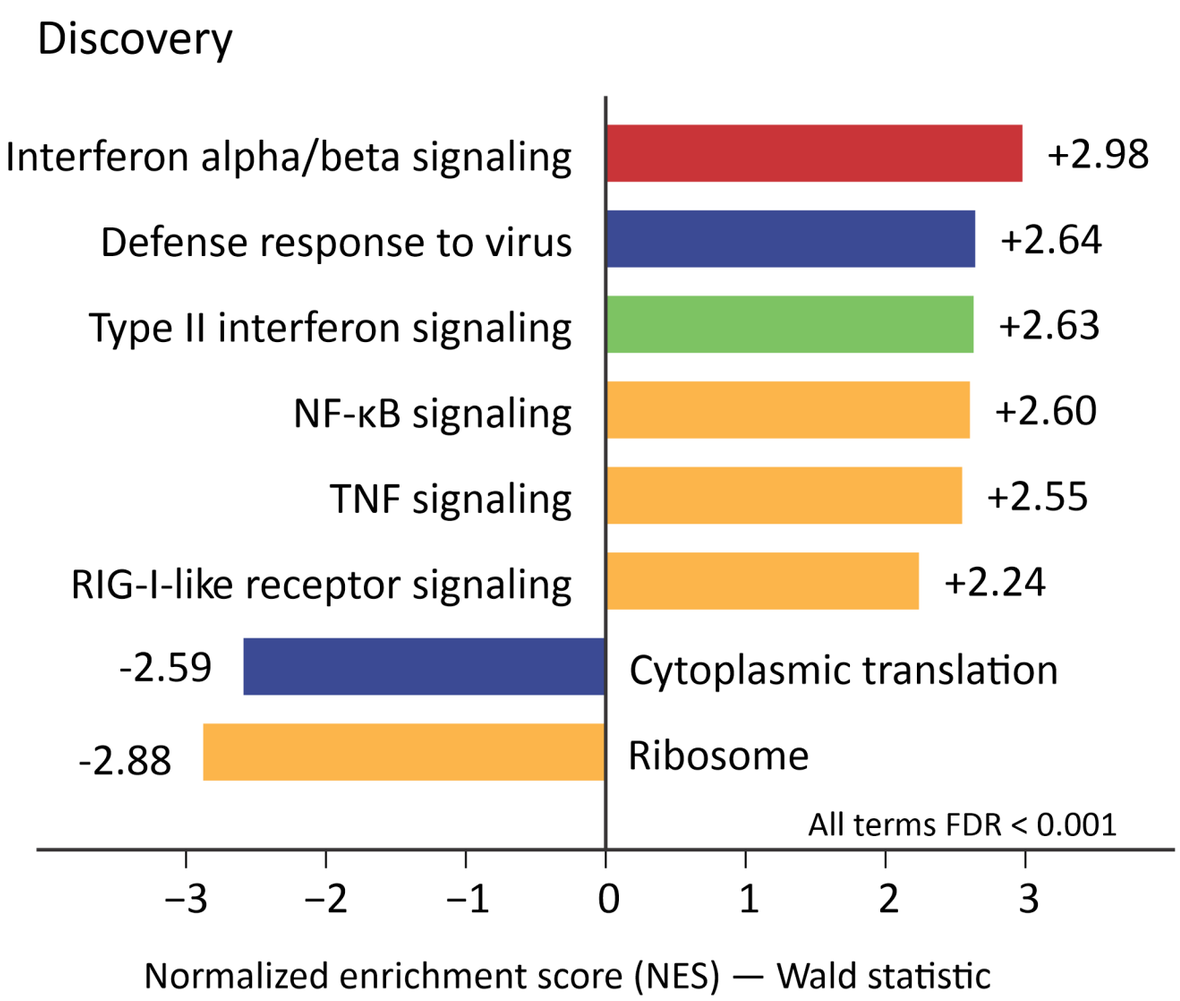
z-score (VST)

A

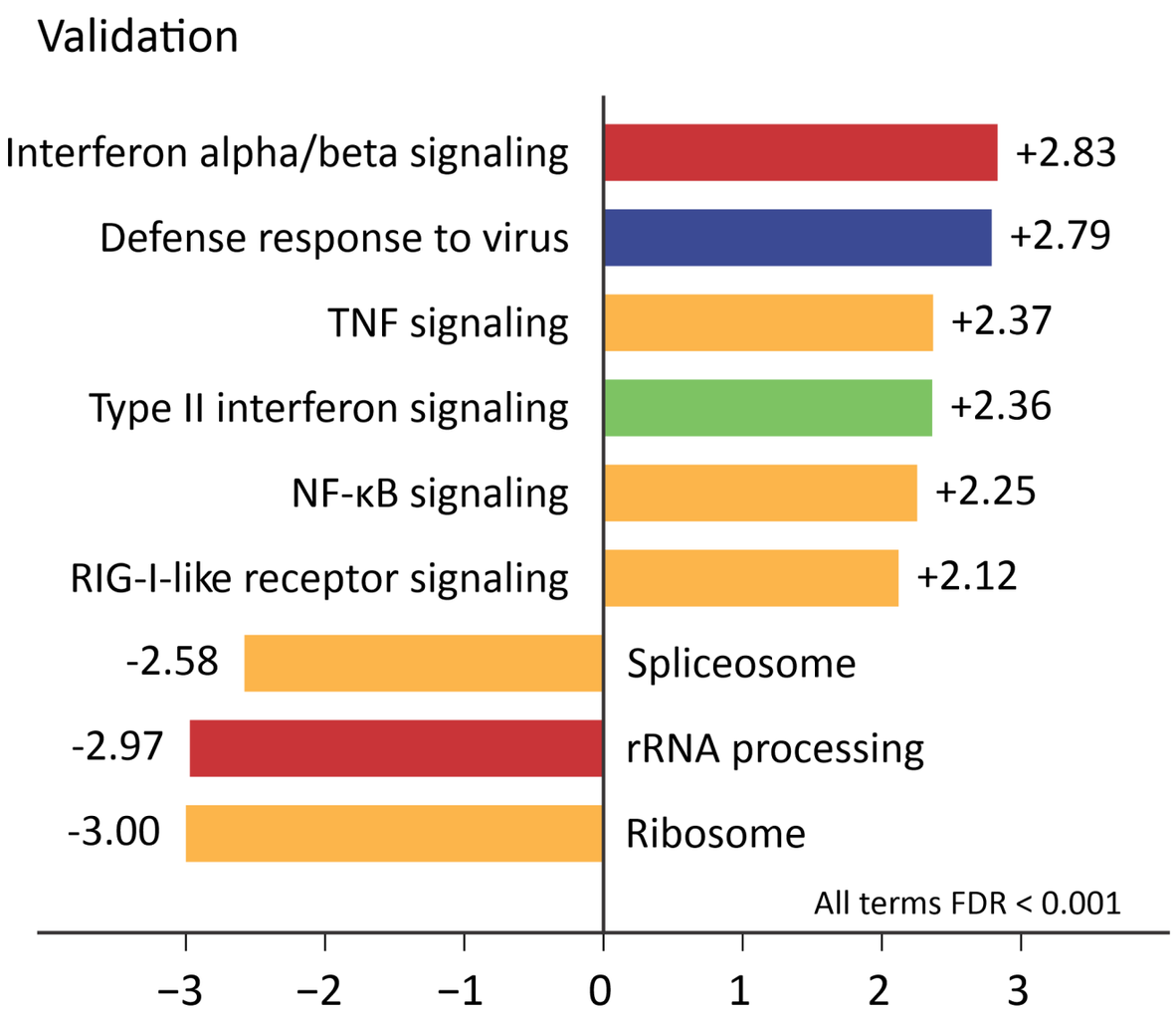


-log10 (Adjusted P-value)

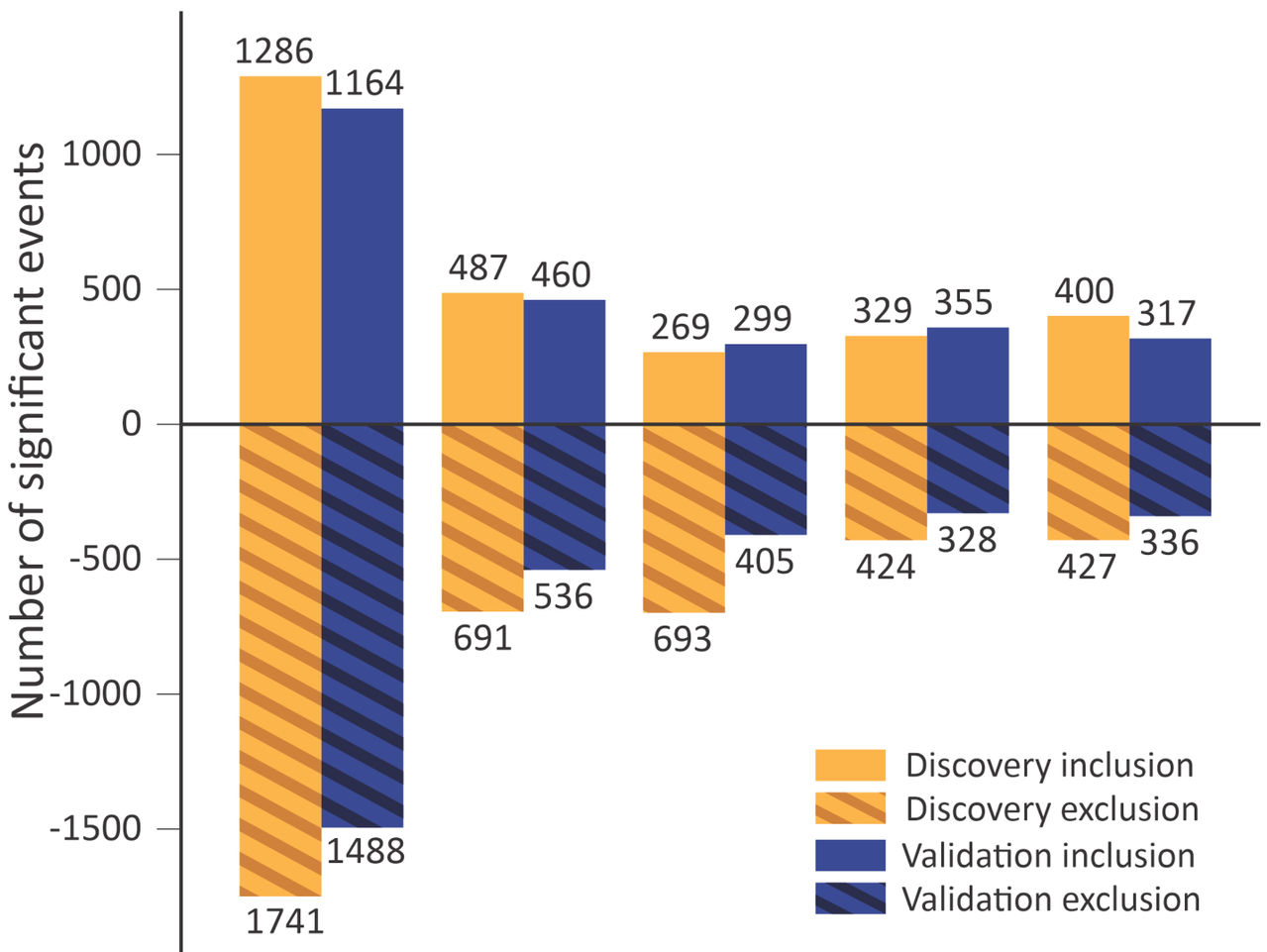
B



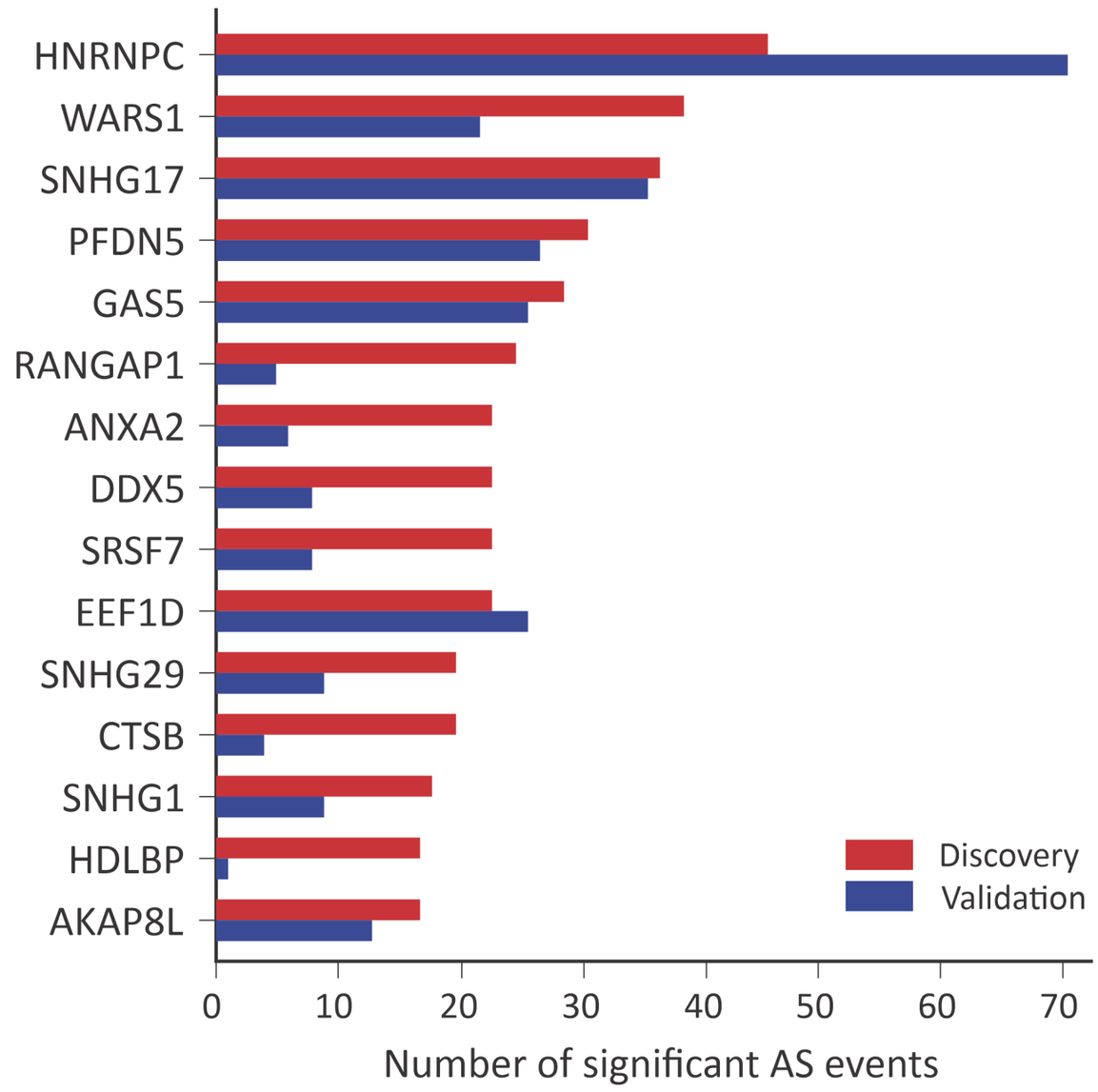
C



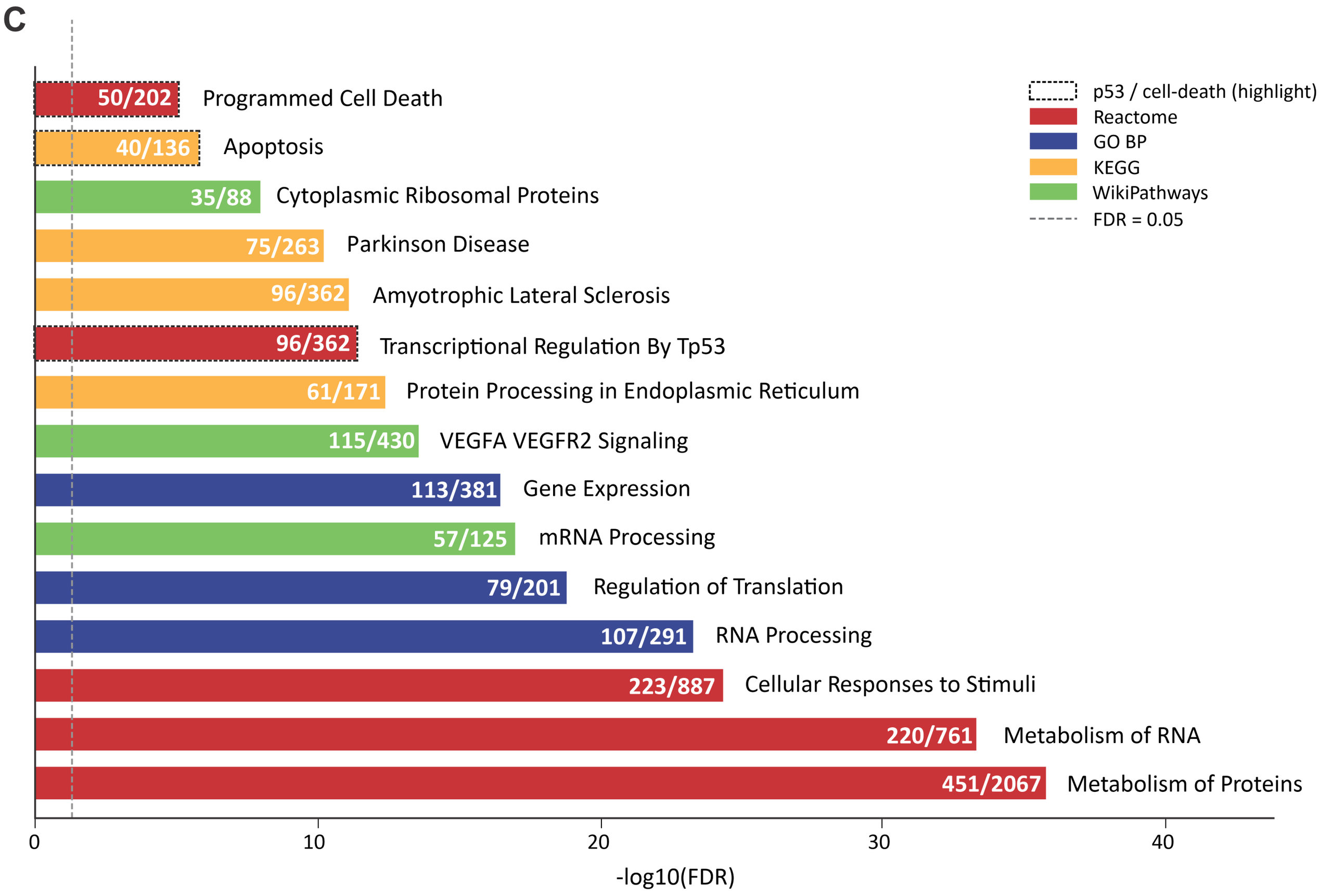
A


Number of significant events
1000
500
0
-500
-1000
-1500
1286
1164
487
460
269
299
329
355
400
317
1741
1488
691
536
693
405
424
328
427
336
Discovery inclusion
Discovery exclusion
Validation inclusion
Validation exclusion
SE
RI
A5SS
A3SS
MXE

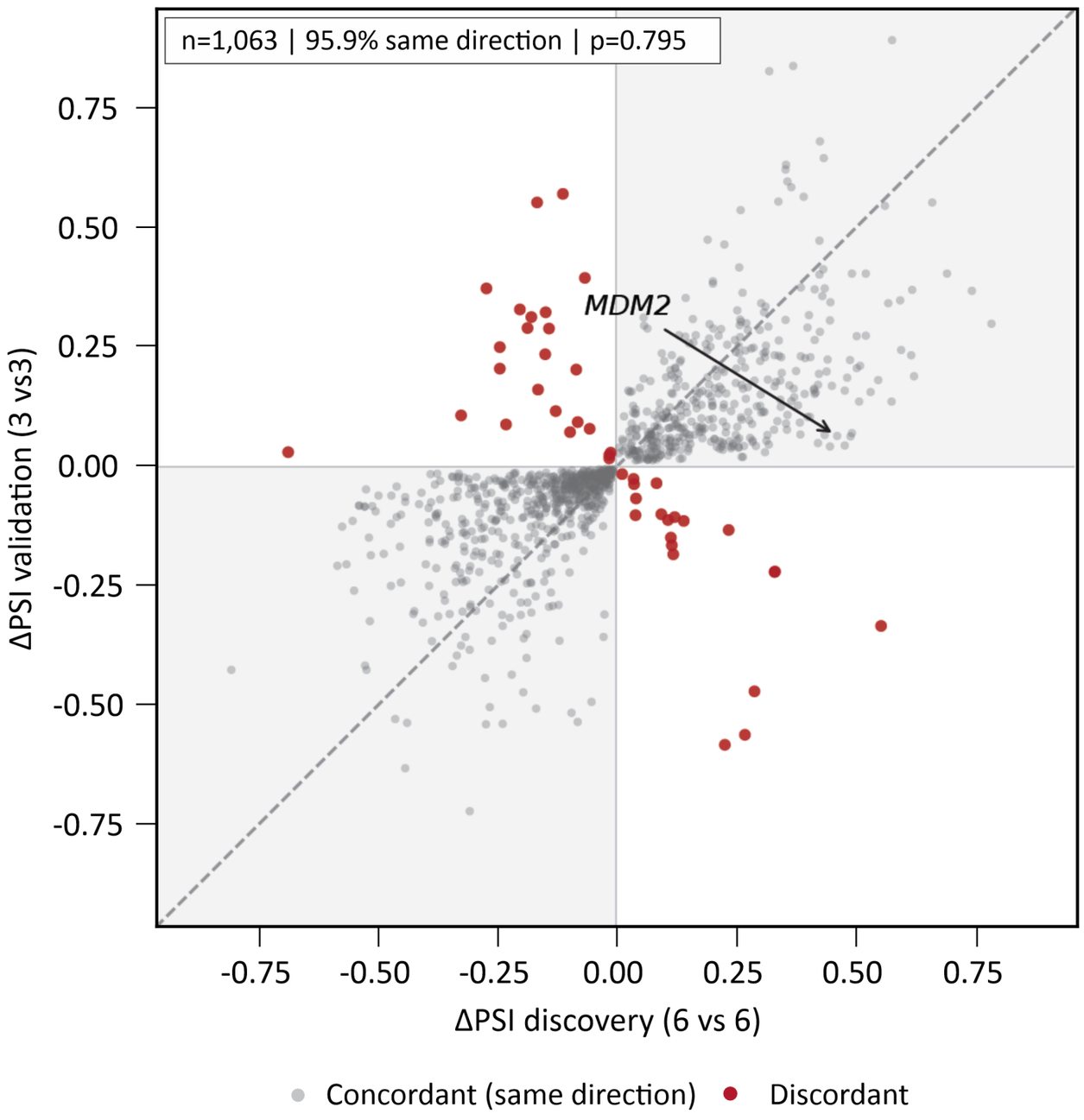
B


HNRNPC
WARS1
SNHG17
PFDN5
GAS5
RANGAP1
ANXA2
DDX5
SRSF7
EEF1D
SNHG29
CTSB
SNHG1
HDLBP
AKAP8L
Discovery
Validation
0
10
20
30
40
50
60
70
Number of significant AS events

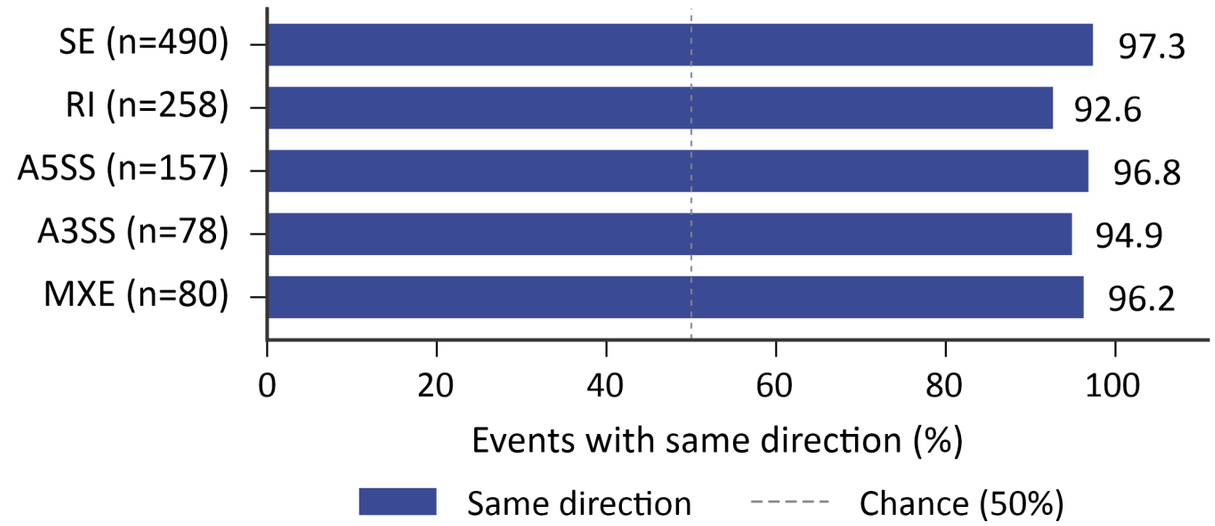
C


50/202
Programmed Cell Death
40/136
Apoptosis
35/88
Cytoplasmic Ribosomal Proteins
75/263
Parkinson Disease
96/362
Amyotrophic Lateral Sclerosis
96/362
Transcriptional Regulation By Tp53
61/171
Protein Processing in Endoplasmic Reticulum
115/430
VEGFA VEGFR2 Signaling
113/381
Gene Expression
57/125
mRNA Processing
79/201
Regulation of Translation
107/291
RNA Processing
223/887
Cellular Responses to Stimuli
220/761
Metabolism of RNA
451/2067
Metabolism of Proteins
p53 / cell-death (highlight)
Reactome
GO BP
KEGG
WikiPathways
FDR = 0.05
0
10
20
30
40
-log10(FDR)

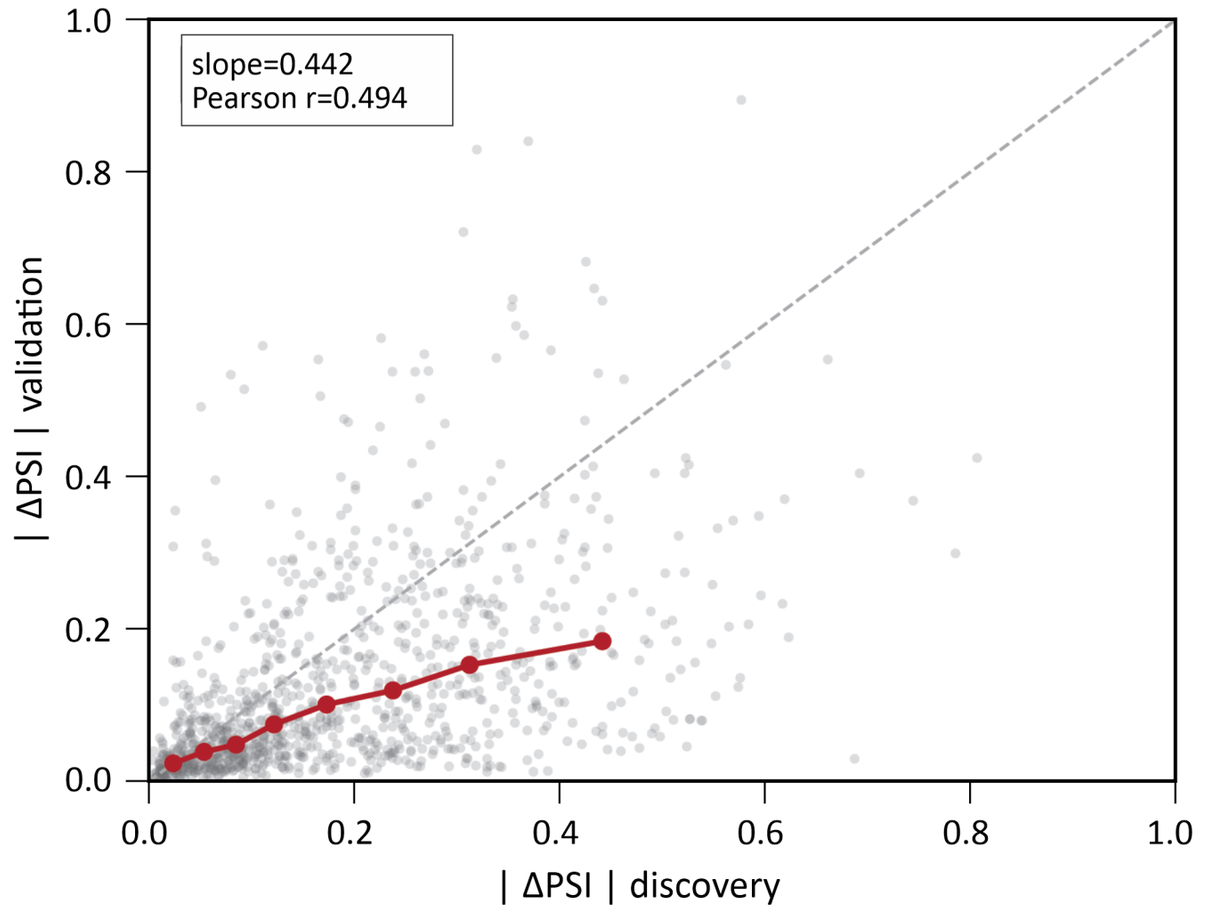
A

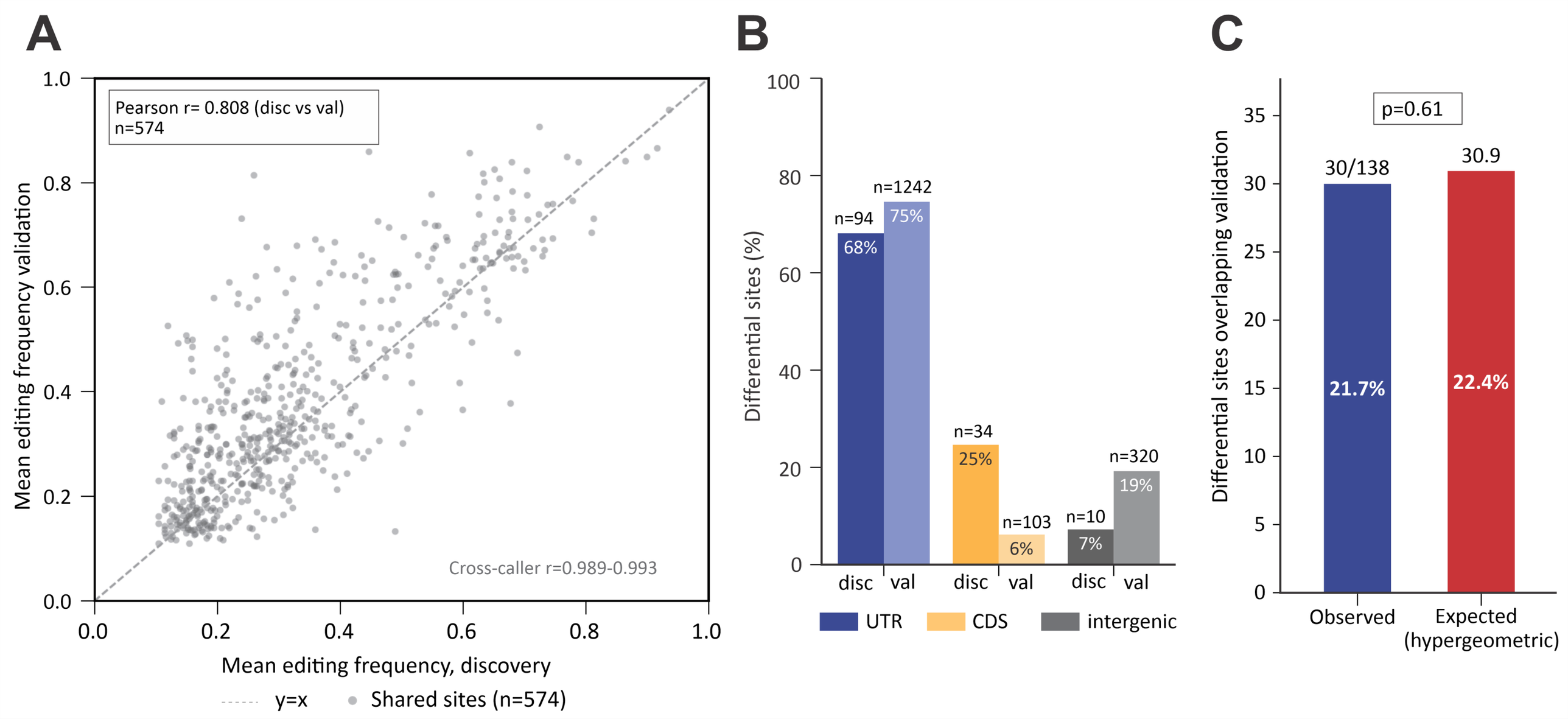

n=1,063 | 95.9% same direction | p=0.795
MDM2
0.75
0.50
0.25
0.00
-0.25
-0.50
-0.75
ΔPSI validation (3 vs3)
-0.75
-0.50
-0.25
0.00
0.25
0.50
0.75
ΔPSI discovery (6 vs 6)
Concordant (same direction)
Discordant

B


SE (n=490)
RI (n=258)
A5SS (n=157)
A3SS (n=78)
MXE (n=80)
97.3
92.6
96.8
94.9
96.2
0
20
40
60
80
100
Events with same direction (%)
Same direction
Chance (50%)

C


slope=0.442
Pearson r=0.494
1.0
0.8
0.6
0.4
0.2
0.0
| ΔPSI | validation
0.0
0.2
0.4
0.6
0.8
1.0
| ΔPSI | discovery
Identity (y=x)
Paired events
Binned medians


A
Pearson r= 0.808 (disc vs val)
n=574
Cross-caller r=0.989-0.993
Mean editing frequency validation
Mean editing frequency, discovery
y=x
Shared sites (n=574)
B
Differential sites (%)
n=94
68%
n=1242
75%
n=34
25%
n=103
6%
n=10
7%
n=320
19%
disc
val
UTR
CDS
intergenic
C
p=0.61
30/138
21.7%
30.9
22.4%
Differential sites overlapping validation
Observed
Expected
(hypergeometric)

p53 pathway ↑

p = 0.0022; q = 0.0043
Δ = +765

ssGSEA score

4400
4200
4000
3800
3600
3400
3200
3000

IFN-α response ↑

p = 0.0022; q = 0.0043
Δ = +2958

ssGSEA score

5000
4000
3000
2000
1000
0

TNF/NF-κB signaling ↑

p = 0.0022; q = 0.0043
Δ = +2681

ssGSEA score

5000
4000
3000
2000
1000

E2F/cell cycle ↓

p = 0.0411; q = 0.0411
Δ = -268

ssGSEA score

5400
5200
5000
4800
4600

Ribosome/translation ↓

p = 0.0152; q = 0.0182
Δ = -334

ssGSEA score

6400
6200
6000
5800
5600

GSC/stemness markers ↓

p = 0.0152; q = 0.0182
Δ = -287

ssGSEA score

8400
8200
8000
7800
7600

Control (n=6)
ZIKV (n=6)

Zika virus

Generic Antiviral Alarm

Post-Transcriptional p53 Release, Intracellular Tug-of-War, and Caspase Execution

Viral RNA

RIG-I / MDA5

Cytokines

↑ proteotoxic/splicing stress

INF I & II

INF Synthesis

STAT2

ISGF3

P

ISG

NS5

STAT2

Proteasome

TNFAIP3
A20

BIRC3
cIAP2

Active p53

NS5

p53

PMAIP1
NOXA

DDIT3
CHOP

A20

ADAR1

cIAP2

ER Stress

NOXA

CHOP

Splicing Machinery

SF3B3

HNRNPC

SRSF2

HNRNPDL

Blocked p53

MDM4

MDM2

p53

MDM2

p53 Brakes

MDM4

pan-caspase response

NS5

Spliceosome

Aberrant Alternative Splicing

Exon Skipping

Intron Retention

Apoptosis
Pyroptosis

Post-Transcriptional Remodeling and Proviral Sequestration.

Supplementary Files

This is a list of supplementary files associated with this preprint. Click to download.

- SupplementaryLegend.docx
- SuplementarFigure1.pdf
- TableS1S7.xlsx